Journal of Electronic Materials
https://doi.org/10.1007/s11664-023-10423-9

ORIGINAL RESEARCH ARTICLE

Short-Range Magnetic Order at Low Temperatures, Exchange Bias, and Negative Magnetization in Undoped $CuCrO_2$

C. Boyraz[1] · P. Aksu[2] · A. Guler[3] · Y. Oner[4] · M. Fujioka[5]

Received: 18 August 2022 / Accepted: 28 March 2023

Abstract

We present the electrical and magnetic properties of polycrystalline $CuCrO_2$ synthesized by solid-state reaction determined to be a hexagonal phase with the space group $R\bar{3}m$. The magnetization measurements have been carried out in the temperature range of 10–400 K, up to a field of 9 T. We observed negative magnetization under a negative internal field induced by the local structural distortions due to the change in the Cr-spin configuration in the CrO_6 tetrahedral. We observed the unidirectional exchange bias field, as well as the magnetization, shift along the magnetization axis at $T = 10$ K and $T = 50$ K, below and above the Néel temperature, $T_N \approx 24$ K. Based on the Modified Langevin function, the magnetization analyses reveal that the local nano-size short-range magnetic ordering forms at the temperatures below the irreversibility temperature, T_{irr} (where the magnetic susceptibility deviates from the high-temperature Curie–Weiss behavior). The nature of the inhomogeneous magnetic state has also been investigated under different approaches such as Griffith's phase. The resistivity measurements were performed in samples with different thermal treatment conditions. It is concluded that the surface of $CuCrO_2$ grains is metallic and magnetically disordered, but the grains inside behave as an ideal antiferromagnetic insulator at lower temperatures. The resistivity measurements were performed in samples with different thermal treatment conditions. It is concluded that the semiconductor $CuCrO_2$ behaves as an ideal antiferromagnetic insulator at lower temperatures.

Keywords Thermo-induced moment · VRH Mott mechanism · negative magnetization · short-range magnetic order · exchange bias · delafossites

Introduction

The delafossite family of compounds is represented by the general chemical formula, $A^{+1}\ B^{+3}\ O^2$, where A and B are metallic cations (A = monocation, B = trivalent transition metal ions). Such a family crystallizes in the layered $R\bar{3}m$ space group. These materials are mostly quasi-two-dimensional and are highly frustrated between neighboring triangular layers as well as within a layer. They are known as multiferroic materials, which are magnetoelectric or ferroelectromagnetic compounds exhibiting both magnetization and dielectric polarization due to the coupling of the magnetic and dielectric ordering (the induction of magnetization by an electric field or the induction of a dielectric polarization by a magnetic field). There are a large number of compounds in this family. Some of the typical examples of triangular antiferromagnetic multiferroic have already been reported by many researchers, such as $CuFeO_2$,[1–6] $LiCrO_2$,[7] and $LiNiO_2$.[8]

✉ C. Boyraz
cboyraz@marmara.edu.tr

1 Department of Mechanical Engineering, Faculty of Technology, Marmara University, 34722 Goztepe, Istanbul, Turkey

2 Institute of Nanotechnology, Gebze Technical University, 41400 Gebze, Kocaeli, Turkey

3 Department of Electrical and Electronics Engineering, Faculty of Technology, Marmara University, 34722 Goztepe, Istanbul, Turkey

4 Department of Physic Engineering, Faculty of Science and Letters, Istanbul Technical University, 34469 Maslak, Istanbul, Turkey

5 Laboratory of Nanostructured Functional Materials, Research Institute for Electronic Science, Hokkaido University, Kita 20, Nishi10, Kita-Ku, Sapporo 001-0020, Japan

Published online: 27 April 2023

On the other hand, magnetoelectric (ME) multiferroicity is not the only exotic phenomenon exhibited by this family of materials. In particular, the discovery of simultaneous transparency and *p*-type conductivity in $CuAlO_2$ by Kawazoe et al.[9] laid the groundwork for developing transparent optoelectronic devices. These materials have also exhibited other critical applications as well known as transparent semiconducting oxides, luminescent materials, and *p*-type solar cell semiconductors.[10,11]

There has been a large increase in the amount of research in developing the understanding of these multiferroics materials. Delafossite $CuCrO_2$ is one of the candidates for such magnetic ferroelectrics. Crystalline $CuCrO_2$ is a triangular lattice antiferromagnet and belongs to this family. It has attracted great attention owing to its potential application in spintronics and multi-state memory devices.[12,13] $CuCrO_2$ is an archetypal material of a frustrated triangular lattice antiferromagnet, which is known to show geometric magnetic frustration due to the antiferromagnetic interactions between the magnetic trivalent ions Cr^{3+}. Such a triangular geometric spin arrangement leads to a disordered, macroscopically degenerate ground state. These all contain antiferromagnetic interactions that are frustrated by the triangular geometry of the lattice. The competition between the near-neighbor and further-neighbor interactions causes frustration which may be seen in antiferromagnets on a two-dimensional (2D) triangular lattice or a three-dimensional (3D) stacked-triangular (simple hexagonal) lattice. It consists of two-dimensional triangular layers stacked along an orthogonal direction. The latter type of frustration may be realized in helimagnets, where a magnetic spiral is formed along a certain direction of the lattice. This geometry does not allow the existence of any spin configuration, simultaneously satisfying all the interactions between the spins. Due to the weak interlayer interaction, the material behaves as a quasi-two-dimensional magnet, which makes it even more interesting.[13–15] $CuCrO_2$, as a multiferroic geometrically frustrated triangular antiferromagnet and exhibits a multitude of magnetic phases associated with structural changes. Based on a microscopic point of view, the ferroelectricity in $CuCrO_2$ can be understood in terms of the scenario introduced by Arima.[16] According to this model, the proper-screw spiral spin order in a low-symmetry crystal can induce ferroelectricity through a variation in the metal–ligand hybridization with spin–orbit coupling. Here, ferroelectricity can be induced by unconventional magnetic ordering arising from geometrical magnetic frustration and breaking spatial inversion symmetry in crystals.[17–19] Since frustrated structures are highly sensitive to external fields and any changes in the magnetic structure can alter the ferroelectricity, the application of magnetic fields may reveal several new magnetic and ferroelectric phases.[20–23] It is suggested to read the study reported by Ledue et al.[24] and references therein. $CuCrO_2$ forms a rhombohedral lattice where the edge-shared CrO_6 layers are alternatively stacked between Cu^+ layers along the *c*-axis.[25,26] The magnetic properties of $CuCrO_2$ have been investigated by neutron diffraction experiments.[26,27] The authors have proposed that the ground state of $CuCrO_2$ exhibits a spinchiral out-of-plane 120° spin structure in which three spins on a triangle form a 120° angle to each other and to the spiral plane parallel to the (110) plane, which is normal to the triangular lattice plane. It was shown that the magnetic configuration of $CuCrO_2$ below T_N is a proper screw with an incommensurate propagation vector pointing along the[28] direction. The magnetic properties are dominated by Cr^{3+} ions ($3d^3$, $S = 3/2$) forming triangular lattice plans and are well represented by an $S = 3/2$ Heisenberg triangular lattice antiferromagnet. A single crystal of $CuCrO_2$ undergoes two successive magnetic phase transitions at $T_{N2} \approx 24.2$ K and $T_{N1} \approx 23.6$ K, respectively. It was found that ferroelectric polarization along the triangular lattice plane develops at T_{N1}. A collinear antiferromagnetic structure occurs first, and then the out-of-plane 120° spin structure forms with decreasing temperature.[27]

Substituting metals such as Mg, Ti, V, Mn, Fe, Co, Ni, Zn, Ga, Rh, and Al ions for the Cr ions is an effective way to change the electrical, magnetic, optical, and thermal transport properties and can induce novel magnetic phenomena. Despite the slight change in their charge carrier density, the magnetic and transport properties show a very sensitive dependence. A very striking result follows from low Mg^{2+} doping, which strongly impacts the transport properties without inducing changes in the magnetic structure. The lowest conductivity can be achieved by doping Mg in the $CuCrO_2$ family.[29–35]

As for the magnetic state of doped $CuCrO_2$, ferromagnetism was realized in hole-doped $CuCr_{1-x}(Mg, Ca, Al)_xO_2$,[30,36] $Cu(Cr_{1-x}Rh_x)O_2$,[37,38] $Cu(Cr_{1-x}Co_x)O_2$,[39–41] $Cu(Cr_{1-x}Al_x)O_2$,[42–44] $Cu(Cr_{1-x}Ni_x)O_2$,[45,46] $Cu(Cr_{1-x}Mn_x)O_2$,[47–50] $Cu(Cr_{1-x}Fe_x)O_2$,[51,52] $Cu(Cr_{1-x}Ti_x)O_2$,[53–57] $Cu(Cr_{1-x}Zn_x)O_2$,[58] and $Cu(Cr_{1-x}Sc_x)O_2$.[59] A spin glass state has been observed by the substitution of V^{3+} for Cr^{3+} substitution in the $CuCr_{1-x}V_xO_2$ for $x > 0.18$.[60,61] Similarly, nonmagnetic Al-doped systems give spin glass behavior.[62] The spin glass state and enhanced spiral phase have also been observed in the disorder induced by V/Al doping in $CuCrO_2$.[63]

There is also a recent review paper on the delafossite oxide $CuCrO_2$ where you can read (i.e., survey) related works including the chemical disorder effect, dilution of the magnetic exchange, and itinerant holes produced by substitutions on its magnetic state.[64] Very recently, Bai et al. presented an account of the efforts in predicting and understanding the optoelectronic properties of the $CuCrO_2$ delafossite oxide.[65]

In this paper, we extend our investigation of the complex magnetic behavior in $CuCrO_2$. Much work on the magnetization of $CuCrO_2$ has been carried out, yet there are still some critical issues. We demonstrate how magnetic clusters evolve from paramagnetic states to long-range antiferromagnetic states. A temperature-dependent scenario of the complex magnetism of $CuCrO_2$ is presented. This work may provide a better understanding of the system concerning how short-range antiferromagnetic clusters exist with the paramagnetic matrix in between the pure paramagnetic and the antiferromagnetic transition temperatures of the system. These nano-sized clusters behave as a weak ferromagnet due to the thermo-induced magnetic moments. We also used a simple model considering the superparamagnetism state in this compound to reveal the role of local short-scale correlations in the mechanism of the observed negative magnetization at low temperatures in the presence of low fields.

The resistivity measurements have been studied in detail to better understand the temperature dependence of the electric transport properties of this compound. It is demonstrated that this compound becomes a perfect antiferromagnetic insulator at lower temperatures, and also investigated how the resistivity changes under different thermal treatments. The complex magnetic states in the intermediate temperature range are discussed in detail, and a temperature-dependent scenario of the complex magnetism of $CuCrO_2$ is presented. This work may provide a better understanding of the system about how short-range antiferromagnetic clusters exist with the paramagnetic matrix in between the pure paramagnetic and the antiferromagnetic transition temperatures of the system.

Materials and Methods

Highly pure (99.999%; Sigma-Aldric) Cu_2O and Cr_2O_3 chemicals were mixed in an agate mortar for redox reaction ($Cu_2O + Cr_2O_3 \rightarrow 2CuCrO_2$) to obtain the $CuCrO_2$ composition. For better atomic packing, the mixture was sintered in a furnace by slowly increasing the temperature to 900 °C. In the first sintering procedure, the samples were kept at 900 °C for 2.5 h, and the temperature was gradually decreased to room temperature by switching off the furnace. Then, the sample was taken out and subject to grinding in an agate mortar and sintered for a second time. Four °C/min increments were applied to reach the maximum 1000 °C second sintering temperature, and the sample was kept at that temperature for 3 h. The sample was then released from the furnace at room temperature. x-ray diffraction (XRD) measurements were performed using a Rigaku Multiflex XRD instrument using a monochromatic Cu Kα (1.5418 Å) source with the 2θ scan rate of 10°–90° to observe the structural phase pattern of the obtained $CuCrO_2$ (see the supplementary material and Figure S1). To clarify the surface morphology and elemental composition of the final $CuCrO_2$ sample, high-angle annular dark-field scanning transmission electron microscopy and energy dispersive x-ray spectrometry were used (see the supplementary material Table S1 and Figure S2). Before performing the resistivity measurements, the pressed rectangular-shaped bulk sample (at 4 GPa) was subjected to surface polishing. Resistivity measurements with the four-probe technique were performed in the temperature range of 5–300 K using a Keithley 6221-type current source (± 2 nA to ± 100 mA), HP 3458A V multimeter (max. 10–8 V), and Lakeshore A340 (1.4–475 K) temperature control device with a carbon glass thermometer. Magnetization measurements as a function of magnetic field and temperature were performed by a vibrating sample magnetometer (PPMS; Quantum Design) in the magnetic file up to ± 9 kOe.

Results and Discussion

Magnetization

Figure 1 shows ZFC (zero-field-cooled) and FC (field-cooled) magnetization as a function of temperature in the applied magnetic field of 5 mT, 50 mT, 0.5 T, and 9 T, respectively. We observed a deviation in $\chi^{-1}(T)$ behavior from the Curie–Weiss law. The inverse susceptibility, $\chi^{-1}(T)$, varies systematically from linear behavior at higher temperatures to non-linear behavior, having negative deviation from Curie–Weiss behavior except for $H = 9$ T, but it deviates positively at lower temperatures. The anomalous behavior of the $\chi^{-1}(T)$ will be handled by different scenarios, such as the magnetic state in the presence of an assembly of antiferromagnetic and ferromagnetic nano-domains coupled to each other by dipolar interactions or Griffiths phase (GP)-like behavior at low temperatures. The magnetic state of the sample may be understood qualitatively using the Langevin function, as discussed below. In the paramagnetic regime, $\chi^{-1}(T)$ versus T curves are fitted to the robust straight line. This yields the best fitting parameters leading to estimating the effective moment of magnetic Cr atoms, μ_{eff} in terms of μ_B/Cr, and the Curie–Weiss temperature, θ_{cw}(K). The values of these parameters are summarized in Table I for all measuring field values, and are also indicated in the figures depicted in the insets of Fig. 1.

It should be noted that $\mu_{\text{eff}} = 3.8\ \mu_B$/f.u. for $H = 90$ T decreases to 2.89 μ_B /f.u. for $H = 5$ mT and $\theta_{\text{cw}} = 198.7$ K for $H = 90$ T reduces to $\theta_{\text{cw}} = 82$ K for $H = 5$ mT. This behavior may be attributed to the strong spin fluctuations (dynamic m in $CuCrO_2$. This leads us to suggest that it is caused by dynamic susceptibility, which will be suppressed with the increasing field, and the effective field of the

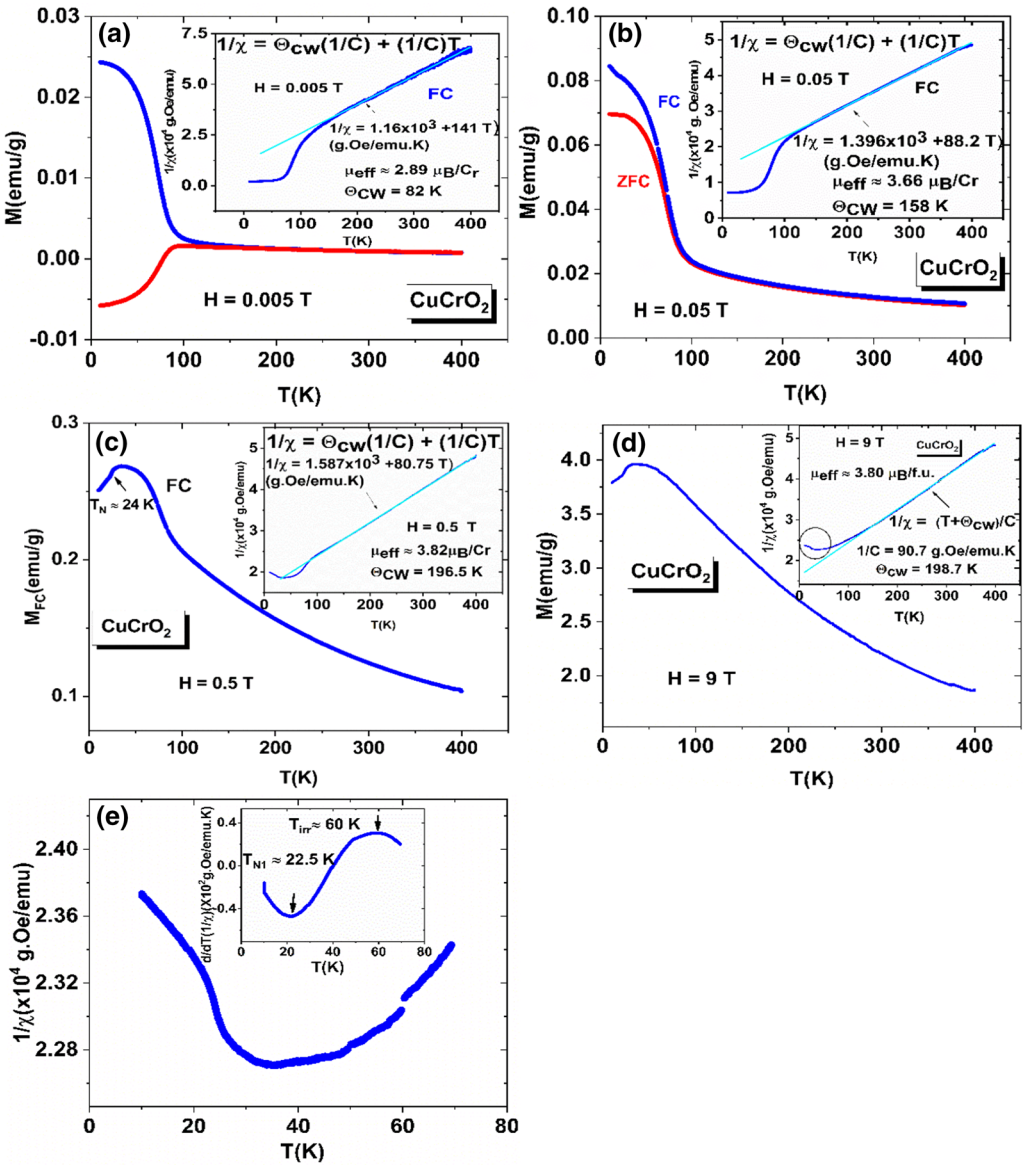

Fig. 1 Zero-field-cooled and field-cooled magnetization as a function of temperature in (a) $H = 0.005$ T, (b) $H = 0.05$ T, (c) $H = 0.5$ T, and (d) $H = 9$ T; insets inverse magnetic susceptibility (χ^{-1}) as a function of temperature showing Curie–Weiss fit in the high-temperature region (solid lines); the figure in the bottom right corner of the inset of (d) displays the magnetization data in detail at low temperatures, while the part circled in the lower left corner in (d) is detailed in (e).

Table I The linear temperature fit of the inverse magnetic susceptibility (χ^{-1}) data to the Curie–Weiss law yields the fitting parameters, the effective magnetic moment, μ_{eff} in terms of Bohr magneton, μ_B per paramagnetic Cr^{3+}, and the Curie–Weiss temperature, θ_{cw} (K)

H (T)	θ_{CW}(T)	μ_{eff} (emu/g)
0.005	82	2.89
0.05	158	3.66
0.5	196.5	3.82
9	198.7	3.80

antiferromagnetic interactions between nearest and next to neighboring Cr atoms acted on the Cr atom site over the measured time of magnetization becomes much stronger. Li et al.[35] have reported that, based on their ESR measurements, the AFM spin fluctuations are extremely strong in the undoped $CuCrO_2$ sample. Distinct bifurcation of the ZFC and FC is also seen in this sample. We observe a huge bifurcation at the low field, here $H = 5$ mT. It starts at around $T_{\text{irr}} \approx 140$ K and decreases with the increasing field, becoming less and less discernible at $H = 0.5$ T and 9 T (not shown in the figure). The most intriguing feature observed is the negative magnetization at $H = 5$ mT. M_{ZFC} has a slight down-turn

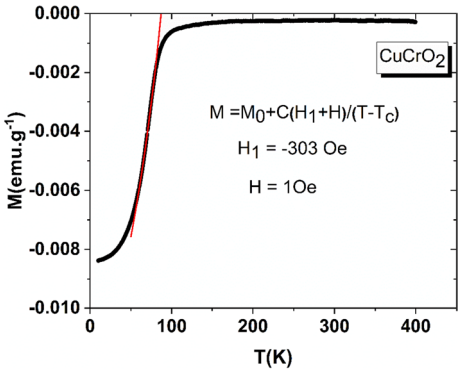

Fig. 2 The cooled field magnetization, $M_{FC}(T)$ in $H \approx 1$ Oe for $CuCrO_2$; the continuous red line shows the fit to Eq. 2. Note that the negative magnetization occurs in the M_{FC} for the fields smaller than the demagnetization field (Color figure online).

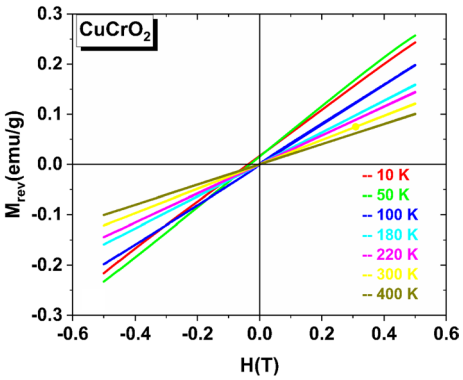

Fig. 4 The reversible magnetization, M_{rev} as a function of the field between $H = \pm 0.5$ T for the selected temperatures indicated.

deviation from linear variation (C–W behavior) below 140 K (T_{irr}) and followed a dramatic drop at around 90 K and then changed its sign from positive to negative, reaching a certain negative level as the temperature is further decreased.

The magnetization reversal becomes more pronounced with the decreasing field, as shown in Fig. 2. Similar negative magnetization has already been observed in some $RCrO_3$ perovskite systems and some perovskite-type complex oxide systems.[66–78] The transition from the paramagnetic phase to the antiferromagnetic phase occurs at around 24 K (consistent with those reported earlier),[29] as indicated in the figures obtained from the derivative of the ZFC magnetization concerning the temperature. It should be noted that the Néel temperature (T_N) shifts towards lower temperatures with the increase of the applied field, presumably due to lattice distortion. It is shown that the change in the Néel temperature is closely associated with the spin–lattice coupling, when the cation is subject to the crystalline field arising from distorted octahedrally or tetrahedrally surrounding anions with the applied field (Fig. 3).[79]

The other important outcome of this study is concerning the exchange bias observed for the first time in undoped stoichiometric $CuCrO_2$. Figures 4 and 3b present the $M_{FC}(H)$ hysteresis loops at $T = 10$ K and 50 K up to $H = \pm 0.5$ T, respectively. It should be noted that they show a shift in both the horizontal and vertical directions. It has been found that the exchange–bias field can be as large as 0.075 T at 10 K, and 0.05 T at 50 K. The magnitude of the magnetization $M(H)$ in the positive field direction is larger than that in the opposite direction $M(-H)$. The difference between the magnetization, $\Delta M(H) = M(H)\text{-}M(-H)$, is a measure of the number of frozen spins in the initial field direction, indicating

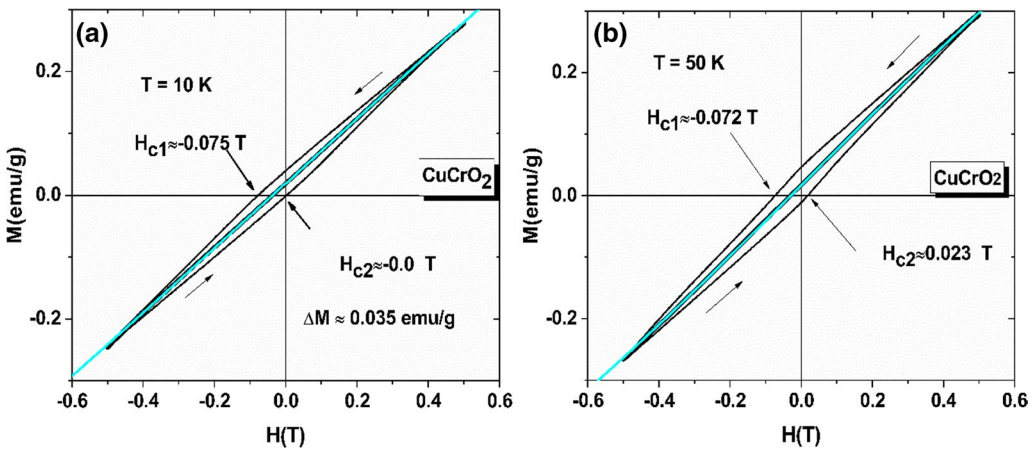

Fig. 3 The FC magnetic hysteresis loops at 10 K and 50 K in (a) and (b), respectively. Both the horizontal and vertical shifts in the FC loop are apparent. The black solid curve between the upper and lower branches of $M(H)$ represents the reversible magnetization, $M_{rev}(H)$. The turquoise solid line is a fitted curve using Eq. 1. The values of H_{c1} and H_{c2}, as indicated in the figure, are the field values crossing the $M = 0$ axis with the ascending (upper) and descending (lower) branches of the M–H loop. The vertical shift ΔM is also given as described in the text. The vertical shift, ΔM, is calculated from the difference between the magnetization values at $H = 0.5$ T.

that the opposite field cannot reverse some spins. The vertical shift may be ascribed to the frozen spins on the surface of the powder samples. The calculated values of, $\Delta M(H)$ are approximately 0.035 emu/g at $T = 10$ K, and 0.028 emu/g at $T = 50$ K. It is noted that all the $M(H)$ loops above 50 K are symmetrical with respect to $M = 0$ axes (see Fig. 4).

It is also worth noting that the uni-directional anisotropy completely loses its rigidity,[80] and that the coercive field is also greatly enhanced in both the zero-field-cooled or field-cooled loops for the field up to $H = 9$ T, as shown in Fig. 5. The observed hysteresis is quite symmetric with the enhanced coercive field as $H_c = 0.13$ T.

Figure 4 shows the magnetic field dependence of magnetization, $M(H)$, at selected temperatures in between 10 K ≤ T ≤ 400 K for −5 T ≤ H ≤ + 0.5 T. The data for $T = 10$ K and 50 K present the reversible component of the (M, H) loops, which is calculated from $M_{rev} = [M+(H) + M-(H)]/2$ where $M+(H)$ and $M-(H)$ are the upper and lower branches of the hysteresis curves. The magnetization curves at temperatures above 50 K are reversible, with no hysteresis varying almost linearly with H. To analyze the magnetization data, we used:

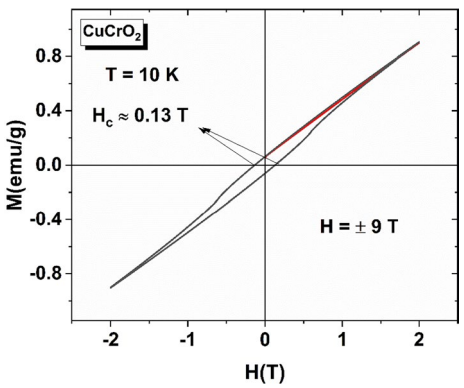

Fig. 5 The FC magnetic hysteresis loops at 10 K are plotted only in the field range between $H = \pm 2$ T to present the observed hysteresis for cooled in $H = 9$ T. Note that the hysteresis is quite symmetrical with an enhanced coercivity compared to $M_{FC}(H)$ loops at low fields for $CuCrO_2$.

$$M = M_s L(x) + \chi H + M_0; x = \mu_{\text{eff}} H/k_B T \quad (1)$$

where $L(x)$ is the Langevin function, $L = \coth(x) - 1/x$, χ is the paramagnetic susceptibility, and M_0 is the temperature-independent term, including the other impurity contribution to the magnetization. Using Eq. 1, the fitting parameters M_s (or μ_s), μ_{eff}, χ, and M_0 are obtained (see Table II).

To demonstrate the quality of fitting, M_{rev} versus H together with the fitting curves are also plotted for $T = 10$ and 50 K, as shown in Figs. 2 and 3. μ_s is the saturation magnetization moment per formula unit (f.u.). If we had measured one unpaired electron per f.u., this would give 1 μs per f.u. We have clearly much less than 3.87 μ_B/f.u. in the temperature range of 10–400 K (this value comes from Cr^{3+} for this compound), as shown in Fig. 6a (the values of the fitting parameters taken from Table II). μ_{eff} comes from the initial slope of the magnetization curve, and is the magnetic moment per independent unit (high spin cluster). The main contribution to the magnetization comes from the second term, χH, which is associated with the paramagnetic moment of the Cr^{3+} atom. From this fitting, we obtain $\mu = 3.53$ μ_B/f.u. and the Curie–Weiss temperature, $\theta_{\text{cw}} = 190$ K. Neither of the estimated values lie too far away from the expected values. Interestingly, the magnetic susceptibility, χ, passes through a maximum at around 90 K, presumably due to the created negative internal field as the temperature is decreased, as shown in Fig. 6b. This behavior provides further evidence for the negative internal field, as discussed below.

Here, we assume that the sample is composed of a number of similar but smaller domains (or clusters) embedded in the paramagnetic matrix inside each grain. There are three different major factors which play an important role in susceptibility. These are antiferromagnetic (AFM) small (nano-size) clusters, paramagnetic Cr^{3+} atoms, and grain surfaces. The first term represented by the Langevin function gives the contribution to the magnetization originating from the small AFM clusters. The small thermo-induced magnetic moments[81] inside the order of the clusters behave

Table II The reversible magnetization, M_{rev} at selected temperatures, $T = 10$ K, 50 K,100 K, 180 K, 220 K, 300 K, and 400 K, is fitted to the equation, $M = M_s L(x) + \chi H + M_0$ with $x = \mu_{\text{eff}} H/k_B T$

Temperature T (K)	M_s (emu/g)	μ_{eff} (μ_B/cluster)	χ (× 10^{-5} emu/g Oe)	M_0 (× 10^{-6} emu/g)
10	0.3245	26.4	2.40	0.0166
20	0.1080	290.0	3.97	0.0142
100	0.0482	907.0	4.04	−3.3
180	0.0466	778.0	2.90	−6.10
220	0.0532	831.0	2.57	−8.20
300	0.0569	995.0	2.10	−10.0
400	0.0370	1301.0	1.80	−8.82

The fitting parameters, M_s(or μ_s) (emu/g), μ_{eff} (μ_B/cluster), χ (emu/g Oe), and M_0 (emu/g) are obtained as summarized in Table II.

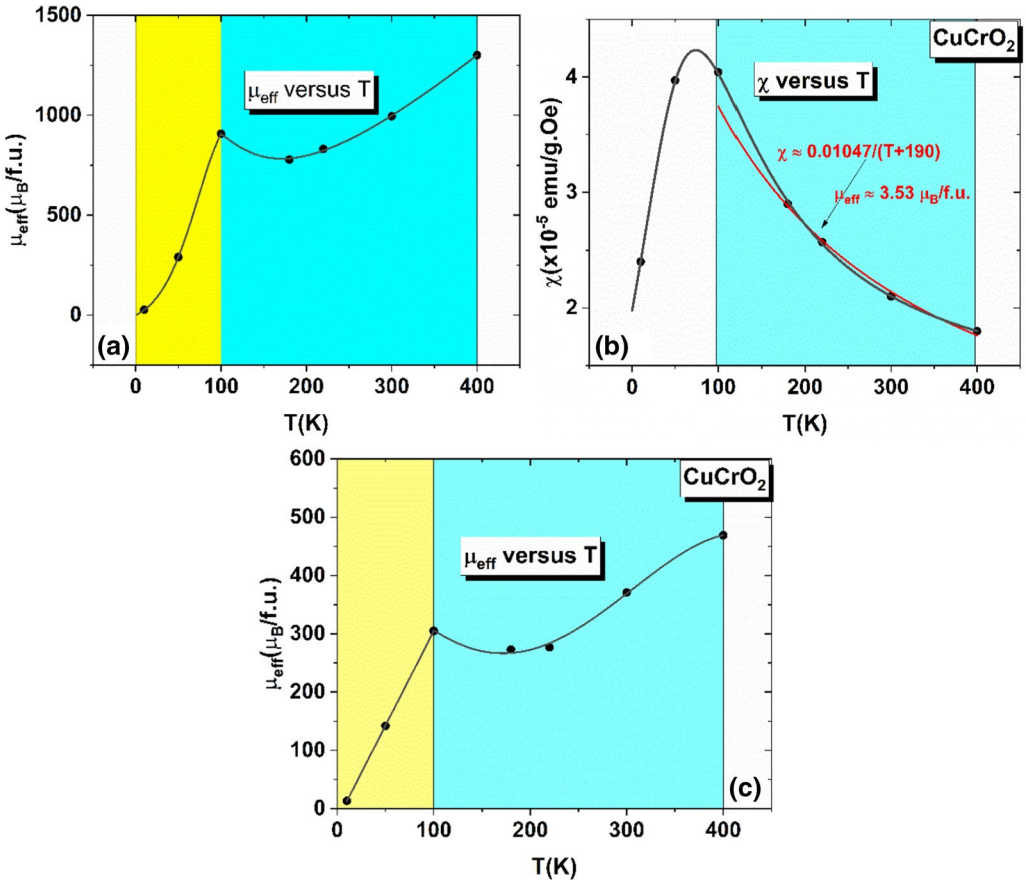

Fig. 6 The fitting parameters of Eq. 1 listed in Table II: (a) the magnetic moment per f.u. at saturation, μ_s , versus temperature, T is shown in two distinct temperature ranges; (b), χ versus T. Note that it passes through a maximum of around 80 K, which confirms the negative internal field. The solid red line shows the fitting to Curie–Weiss's expression; (c) μ_{eff} (μ_B/cluster) versus temperature, T in two distinct regions. Note that μ_{eff} increases almost linearly with temperature below 100 K as being consistent with the prediction for the temperature dependence of thermo-induced magnetic moments (Color figure online).

as a weak ferromagnet. This behavior has been supported by the outcome of the susceptibility measurements. The fitting parameter, μ_{eff} varies exactly linearly with temperature, T up to $T = 100$ K, as shown in Fig. 6c, being consistent with the linear temperature behavior of the thermo-induced AFM moments inside the cluster. This is in accordance with the susceptibility of ferrihydrite nanoparticles.[82] As the temperature is further increased, then μ_{eff} stays almost constant in the intermediate temperature range. It should be noted that the average net moment over a small cluster size due to uncompensated spins will be much smaller than that obtained from thermo-induced magnetic moment prediction. In general, the total magnetic moment of an antiferromagnetic nano-size region is expected to have contributions from both uncompensated spins and a thermo-induced moments. However, we ignore the contribution of the uncompensated moments.[83]

A negative magnetization and its coexistence with a negative exchange bias have been observed in many similar systems. For example, an orthochromite $GdCrO_3$,[66,67] $LaCr0_{.85}Mn_{0.15}O_3$, $NdCr_{1-x}Mn_xO_3$, $LaCr_{0.8}Mn_{0.2}O_3$,[70–72] Fe-doped $CoCr_2O_4$,[74] Cr doped Co_2TiO_4,[75] $Ni_{5.33}Ta_{0.67}B_2O_{10}$[76] exhibited a magnetization reversal due to a negative internal field, and has taken a special place as an interesting series of compounds in this respect. The phenomena observed in all these compounds are explained based on the competition of the two magnetic sublattices. Firstly, Cooke et al.[66] suggested that the interaction between the Cr^{3+}(AFM sublattice) and Gd^{3+} (PM sublattice) ions produces an effective field at the Gd sites, acting in the opposite direction as a created negative field. A weak ferromagnetic component perpendicular to the chromium sublattice magnetization arises from canting of Cr moments away from strictly antiferromagnetic alignment. The origin of spin canting is attributed to an antisymmetric exchange interaction, as discussed by Dzyaloshinski and Moriya.[84] Using the same two-magnetic sublattice model, Yoshii also investigated the magnetic state of the perovskite $GdCrO_3$[67] and $La_{1-x}Pr_xCrO_3$.[68] The negative magnetization observed in $(La_{0.3}Pr_{0.7})_{1-x}Ca_xCrO_3$ ceramics has been explained by Huang et al.[73] Recently, Tripathi

et al.[77] have discussed the role of local short-scale correlations in the mechanism of negative magnetization in the antiferromagnetically ordered $GdCrO_3$. In $GdCr0_3$, the Cr ions order antiferromagnetically near 170 K. In addition to antiferromagnetism, a weak ferromagnetic component perpendicular to the Cr sublattice magnetization arises from canting of Cr moments. The origin of spin canting can be attributed to an antisymmetric exchange interaction, as discussed by Dzyaloshinski and Moriya. The ordered Cr system produces an internal field that is opposite in direction to the ferromagnetic component of the Cr moment.

It is seen that the phenomenon of negative magnetization is not limited to one type of compound, such as perovskite only, but can also be observed in other systems having an antiparallel ordering between two (or more) ferromagnetic sublattices corresponding to the different crystallographic sites. We suggest the reader read the review article by Kumar.[78] It is likely that this model is applicable only to the substances comprising two and more magnetic sublattices. However, Tripathi et al.[77] have pointed out that the observed negative magnetization depends on the thermal history of the sample for antiferromagnetically ordered $GdCrO_3$, causing the validity of the two competing sublattice models in the microscopic view. In fact, the negative magnetization findings need to be interpreted with caution even in the case of getting a better fit to the experimental data using the suggested fitting formula. Microscopic approaches for understanding the origin of the negative internal field have brought encouragement using the negative internal field terminology to interpret the negative magnetization observed in the system having only one magnetic lattice. Zhao et al.[85] have demonstrated that the oxygen octahedral tiltings in RMO_3 perovskites play an important role. The coupling of the R and M magnetic moments with the oxygen octahedral tilting gives an effective magnetic field acting on the R atoms, thereby paving the way to explain several intriguing features of these compounds, for example, a compensation temperature displayed. As for $CuCrO_2$, we speculate that the superexchange interaction Cr^{3+}-O^{2-}-Cr^{3+} due to CrO_6 octahedra tilting in the ab plane may produce a negative internal field on a paramagnetic Cr site, because a weak ferromagnetic superexchange interaction is also present due to the nearly 90° Cr-O-Cr bond in the edge-shared CrO_6 octahedra. Therefore, we can also adopt the negative internal field terminology and apply it to our undoped $CuCrO_2$ compound. We use the following equation to fit the magnetization curves:

$$M = M_0 + C(H + H_1)/(T - \theta_c) \tag{2}$$

Here, M_0, C, H_1, H, and θ stand for the temperature-independent magnetization, including the magnetization $M(-H_1)$ and impurity effects, a Curie constant, an internal field from Cr^{3+}, an applied field (it is assumed to be temperature-independent for first-order approximation in the fitting temperature range), and a Weiss temperature, respectively.

By fitting the $M_{ZFC}(T)$ data at $H = 50$ Oe (see Fig. 7a) using Eq. 2, the parameters are obtained as -8.1×10^{-3} emu/g, 8.6×10^{-3} emu.K/g Oe, −70 Oe, and 98 K, respectively. We have determined the magnetization of $CuCrO_2$ from the initial $M(H)$ curves to be M (50 Oe) ≅ 0.01 emu/g, very close to the value obtained from the fitting, M_0. The relationship of $M = M_{Cr}$ is almost satisfied below T_N (~ 24 K) when H is equal to $-H_1$. The paramagnetic Cr^{3+} moment can be calculated from the Curie constant C, which was $\mu_{eff} \approx 3.2\ \mu_B$/Cr. For the Langevin fit to the magnetization at $T = 10$ K, the effective magnetic moment for Cr was found to be 3.53 μ_B/Cr (as given above), not too far from this fair value. As for the Curie temperature, the interaction between Cr atoms favors ferromagnetic alignment. In the paramagnetic regime at a temperature above 150 K, the Curie temperature has a tendency to antiferromagnetically align (~−190 K). The fitting shows the negative internal field as $H_1 = -70$ Oe.

To emphasize the negative internal field effect on the susceptibility, we also analyzed M_{ZFC} versus T data for $H = 0.05$ T and $H = 0.5$ T. Figure 7b and c show the susceptibility $\Delta M_{net}(T)$ data after subtracting the magnetization obeying Curie–Weiss behavior from the M_{ZFC} measured data. As shown in the figures, both curves begin to rise at around 100 K, and then pass through a maximum at $T \sim 35$ K for $H = 0.05$ T, and $T \sim 60$ K for $H = 0.5$ T, indicating that two competing factors play a role in the magnetization. As we have argued above, short-range antiferromagnetic order develops inside the grains and acts as a weak ferromagnet due to the thermo-induced moments in the field. It should be noted that the thermo-induced moment per Cr atom is much stronger than that of the uncompensated spins. The other factor gives a negative magnetization, which is attributed to the paramagnetic susceptibility of the Cr atoms. The internal negative field produces a magnetization (M) in the opposite direction to that of the applied field. However, if we assume that the sample contains a number of smaller (nano-size) but similar ferromagnetic and antiferromagnetic domains distributed randomly inside the micro-$CuCrO_2$ particles in their demagnetized state, the average net magnetic moment can be obtained statistically,[86] and then the combination of these effects lead to:

$$\Delta\chi = \frac{\gamma C}{\left[(T+\theta)\left(1 + n\ \exp\left(-E_{exc}/k_B T\right)\right)\right]} - \frac{(1-\gamma)C_1}{(T+\theta_{cw})} + \chi_0 \tag{3}$$

where it is assumed that there are two distinct states of the domains in the field,. thepr energies being E_1 and E_2, and one defines $E_{exc} = E_1$-E_2. Each state of E_1 and E_2 is assumed to have N_1 and N_2 degeneracy, respectively.

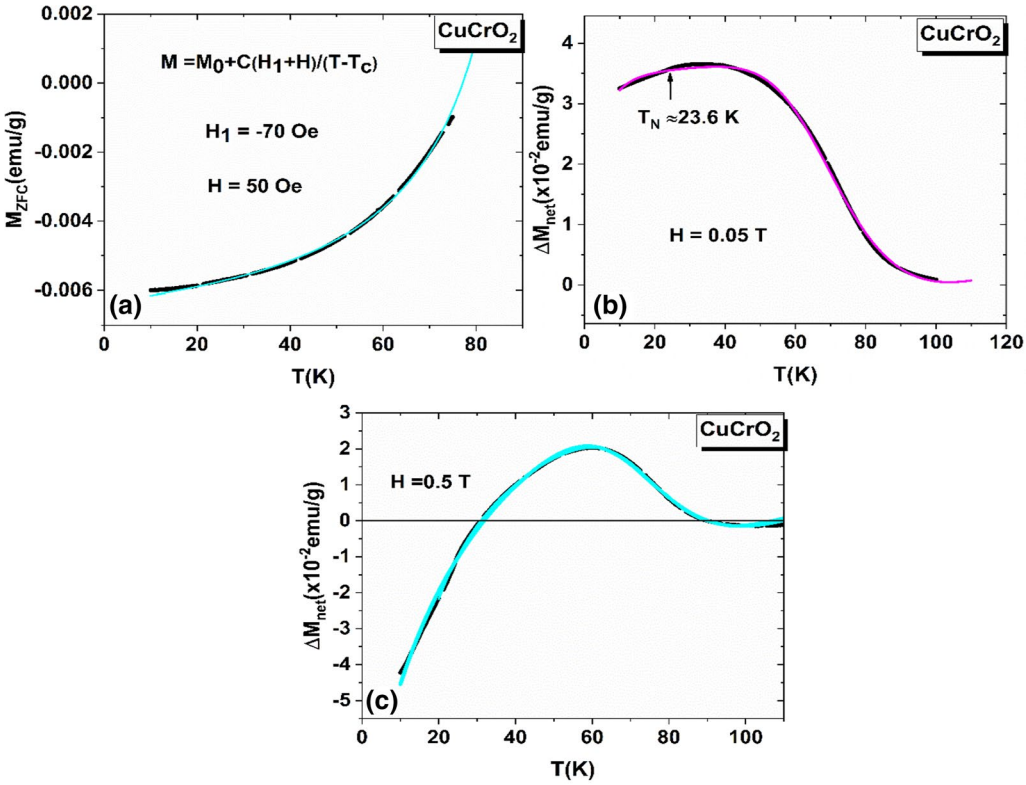

Fig. 7 The magnetization, M_{ZFC} , versus the temperature, T, for the field $H = 50$ Oe; the solid line is the best fit from Eq. 2 in (a). In (b) and (c), the magnetization, ΔM_{net} , versus the temperature, T, after subtracting the high-temperature paramagnetic contribution from the total measured magnetization, $M(T)$ in the ZFC case for the applied fields, $H = 0.05$ T and $H = 0.5$ T, respectively; the continuous line represents the curve fitted to Eq. 3.

$\nu(T) = 1/[1 + (N_2/N_1)\mathrm{Exp}(-E_{exc}/k_BT)]$ is the fractional occupation number of the state E_1, If we suppose that $< \mu_2 >$ is almost zero, where $n = N_2/N_1$, which can be regarded as the ratio of the number of domains. The pre-factor γ denotes the volume fraction of the magnetically ordered region. It is noticed that the number of nano-size antiferromagnetic order regions increases with the decreasing temperature, which means that the magnetically ordered volume fraction varies with temperature, and achieves its maximum value for the temperature at which ν (T) asymptotically approaches 1. The fitting parameters are summarized as follows: $\gamma C = 1.07 \times 10^{-2}$ emu.K/g Oe (corresponding value of the effective moment per cluster, $\mu_s = 3.56\ (\gamma n_s)^{1/2}\ \mu_B$/cluster, where n_s is the number of f.u. per cluster), $C_1 \cong 6.0 \times 10^{-3}$ emu.K/g Oe, which corresponds to $\mu = 2.66\ \mu_B$/f.u., $\theta = 44$ K, $\theta_{cw} = 26.5$ K, $n = 2000$, $E_{exc}/k_B = 585$ K, and $\chi_0 = 3.78 \times 10^{-5}$ emu/g Oe for $H = 0.05$ T; $\gamma C = 2.03 \times 10^{-3}$ emu.K/g Oe (corresponding value of the effective moment per cluster, $\mu_s = 1.57(\gamma n_s)^{1/2}\ \mu_B$/cluster), $C_1 \cong 6.0 \times 10^{-3}$ emu.K/g Oe, which corresponds to $\mu = 2.66\ \mu_B$/f.u., $\theta = 111$ K, $\theta_{cw} = 37$ K, $n = 2800$, $E_{exc}/k_B = 645$ K, and $\chi_0 = 1.07\mathrm{X}10^{-5}$ emu/g Oe for $H = 0.5$ T. Using the values, μ_s (the saturation magnetization moment per f.u.) from Table II and Fig. 6a, the estimated values vary almost linearly with decreasing temperature from 1×10^{-3} to $5 \times 10^{-3}\ \mu_B$/f.u. in our fitting temperature range, while the maximum value of n_s is found to be about $10^6\gamma$ (f.u./cluster), indicating the existence of nano-sized order regions. These analyses reveal that these correlations are most pronounced at low values of the applied magnetic field but become readily suppressed when the fields exceed 0.5 T. It is worth noting that, at a very high field, $H = 9$ T, the deviation of χ^{-1} from Curie–Weiss behavior changes its character from turn-down to turn-up (see Fig. 8).

As a result, $CuCrO_2$ compounds demonstrate an inhomogeneous distribution of the order parameter through the sample in the intermediate temperature range. Octahedral tilting occurs when the cation at the Cr-site is too small to fill the cavity between CrO_6 octahedrons, resulting in the lowering of crystal symmetry. This property raises an interesting question on the natural driving force, which induces lattice distortion. In-plane distortions in $CuCrO_2$ have been observed in high-resolution x-ray diffraction measurements.[79] Kimura et al. suggested two possible scenarios for the origin of the driving for inducing lattice distortions: a spin–lattice coupling in such a frustrated

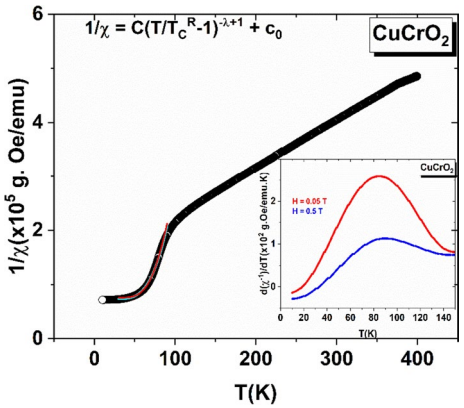

Fig. 8 The inverse susceptibility (χ^{-1}) versus temperature (T) curve for $H = 9$ T. A sharp downturn seen in inverse magnetic susceptibility indicates a phase transition. The continuous lines with different colors show the fit to the modified Curie–Weiss law (red line) and the thermal activated domains' susceptibility [exp (E_a/k_BT)] behavior presented with the cyan line) as described in the text. *Inset* the deviation of χ^{-1} from Curie–Weiss behavior (Color figure online).

state causes a distortion (as inherent to the frustrated system), or it occurs owing to the exchange magneto-striction mechanism. Asymmetry breaking takes place associated with the magnetoelastic stress placed on the triangular lattice through the Cu-O-Cu coupling (interlayers coupling). Upon observation of some intriguing findings, such as a larger effective magnetic moment and large deviation of inverse susceptibility χ^{-1} from Curie–Weiss law in $CuCrO_2$, it is demonstrated whether or not the $\chi^{-1}(T)$ may qualify as GP-like. The χ^{-1} for $H = 0.5$ T is replotted exclusively (see Fig. 8). A possible origin of the non-analytical behavior of χ^{-1} may be attributed to the defects which drive magnetic inhomogeneity, breaking long-range magnetic interactions in the ordered region or inducing local ordering in the paramagnetic matrix. Our experimental results bear a close resemblance to the GP-like behavior (neither reflecting long-range ferromagnetic order nor a pure paramagnetic one).[87] χ^{-1} reveals high-T linear regions corresponding to the paramagnetic phases followed by the downturns. At low-T, the data show another linear region just above T_N (~ 24 K), as seen in Fig. 8. In fact, the temperature derivative d/d$T(\chi^{-1})$ precisely indicates a deviation from the Curie—Weiss law in the GP, as shown in the inset of Fig. 8. The plot of d/d$T(\chi^{-1})$ versus T shows a peak-like feature, between ~ 20 K and 140 K, with a maximum at ~ 85 K and ~ 95 K for susceptibility measured in an applied field of 0.05 T and 0.5 T. The range of temperature over which the peak-like feature in the d(χ^{-1})/dT covers the region where GP is observed. The peak temperature is commonly used to obtain a much better fit. It is noticed that the intensity of d(χ^{-1})/dT reduces with the increasing measuring field, H, it is expected to be suppressed by fields at a much higher field than $H = 0.5$ T and below $H = 9$ T, since the deviation from the linear-T behavior changes its polarity toward a turn-up direction at $H = 9$ T. The suppression by the field is mostly taken as a hallmark of GP singularities. The disappearance of the magnetic contribution arising from the short-range magnetic order with the applied magnetic field has already been observed in some compounds.[88,89] GP is, generally, characterized by a DC magnetic susceptibility exponent (λ) using:

$$\chi^{-1} = \left(\frac{T}{T_C^R} - 1\right)^{1-\lambda}; 0 < \lambda < 1 \quad (4)$$

where a magnetic susceptibility exponent $\beta = 1 - \lambda$. The critical exponent λ represents a downturn deviation from the Curie—Weiss law occurring below the Griffiths temperature T_G. The T_C^R temperature plays a similar role to the paramagnetic Curie temperature Θ in the Curie–Weiss formula $H/M \sim (T—\Theta)$ for the paramagnetic phase. It is always possible to determine the fitting parameters, λ and T_C^R. What is the most convincing way to test GP assertion? We have first applied Eq. 3 for $T_C^R = 95$ K (where d/dT(χ^{-1}) versus T shows a peak at $H = 0.5$ T) to the data, yielding $\lambda = 0.6$ lying in the range of 0 and 1. Relying on this fitting outcome, even though the best fitting takes place in a very narrow interval covering only a few percent of the temperature range between the antiferromagnetic phase below the Neel temperature $T_N = 24$ K and the pure paramagnetic phase above the GP temperature $T_{irr} = 140$ K, it may be taken as evidence of the GP. However, we believe that the most convincing evidence may be obtained if the fitting is handled with the method used by Majee et al.,[90] who recently reported on the investigation of the so-called GP-like in the non-magnetic Ti-doped antiferromagnetic delafossite compound $CuCr_{0.95}Ti_{0.05}O_2$ using Eq. 3 for the susceptibility. However, they have pointed out that, to get unambiguous results, the choice of T_C^R should be such that $\lambda = 0$ in the region above the onset of GP, so that the equation converges to conventional Curie–Weiss law in the paramagnetic phase.

Using the same test, the fitting has been carried out for the different selected temperatures, as shown in Fig. 9. However, we get the best fit at $T_C^R = 30$ K covering a wider temperature range, but this gives $\lambda = -0.45$, an unsuitable value for GP. Therefore, we can safely rule out the presence of GP. Moreover, a sharp downturn seen in inverse magnetic susceptibility fits perfectly (see Fig. 8) to the equation $\chi^{-1} = a^* \exp(-E_g/k_BT) + c$ with $a = 1.36 \times 10^7$ emu^{-1}.g Oe, $E_g/k_B = 420$ K, and $c = 7.5 \times 10^4$ emu-1.g Oe. The result confirms once more the evidence of the presence of thermally activated clusters, as argued above.

As mentioned above, we observed exchange bias manifested by significant shifts of $M(H)$ loops at $T = 10$ K and

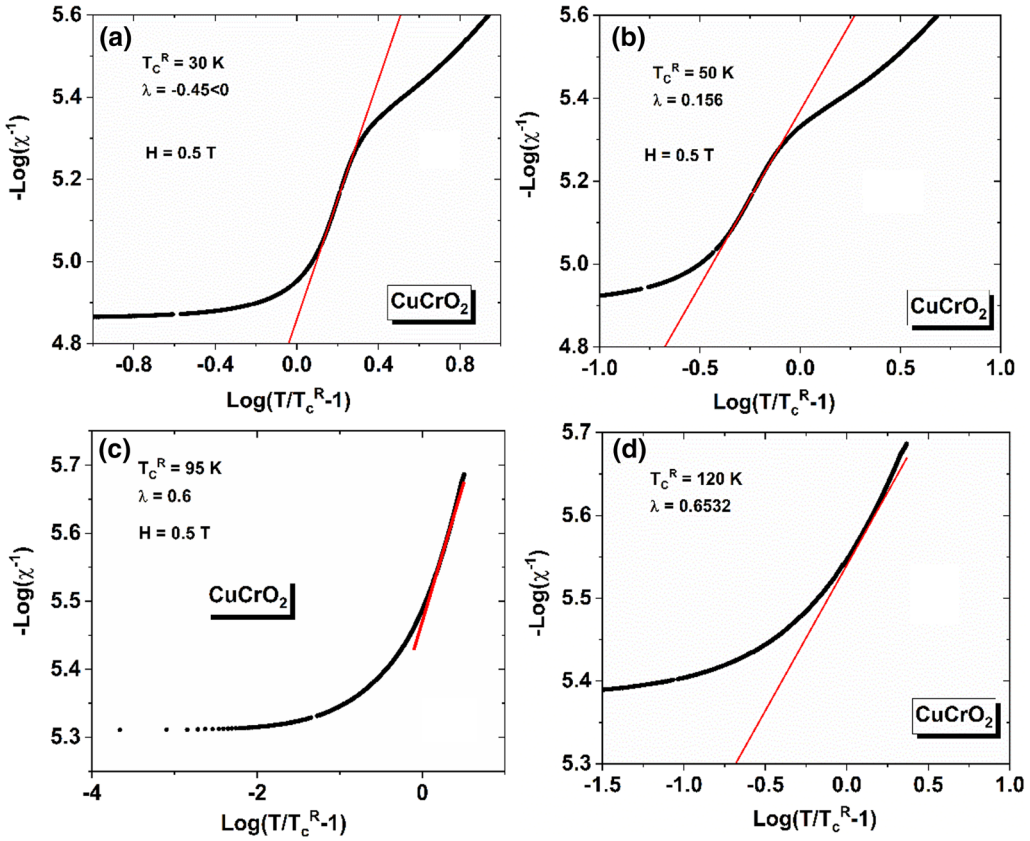

Fig. 9 The susceptibility data are fitted to the modified Curie–Weiss law (Eq. 4) (solid line) for selected values of T_C^R between the Néel temperature, T_N ~ 24 K, and the paramagnetic transition temperature, T_{irr} ~ 140 K: (a) at T = 30 K, (b) at T = 50 K, (c) at T = 95 K, (d) at T = 120 K. The fitting parameter λ is indicated in the figure for each temperature.

50 K in both the horizontal and vertical directions after field cooling from room temperature to the measuring temperature. The exchange bias in $CuCrO_2$ is dependent on the cooling field due to the influence of the magnetic field on the grain surfaces breaking the interfacial exchange interactions induced by the grain surfaces. Usually, exchange bias has been observed in many different systems containing FM (ferromagnetic)/AFM (antiferromagnetic) interfaces, such as inhomogeneous materials, thin films consisting of bilayers, and double superlattices. In addition to FM/AFM interfaces, exchange bias has also been observed in other types of interfaces involving spin glass (SG) and FM or AFM phases, e.g., (AFM, FM/SG) in nanoparticles.[80,91] In some materials, a vertical shift along the magnetization axis in addition to the shift along the field axis also emerges. The existence of the vertical shift of the $M(H)$ loop is most often best exemplified by nanoparticle systems,[92,93] such as with other systems.[94,95] However, they more typically occur in phase-separated systems, for example, in the perovskite cobaltite $La_{1-x}Sr_xCoO_3$. Tang et al.[96] observed magnetization hysteresis loops exhibiting both horizontal and vertical shifts. Exchange bias is strongly dependent on the measuring field and the cooling field, consisting of the change of the relative proportion of the coexisting phases by the external field. However, through the comprehensive study of the exchange bias in polycrystalline FM/AFM films, O'Grady et al. have recently revealed the existence of disordered interfacial spins as "spin clusters" analogous to a spin glass at the interface between the FM and AFM layers.[97] These clusters are believed to transmit the anisotropy from the AFM layer to the FM layer, allowing for interactions via the exchange coupling to the AFM and FM layers that gives rise to the coercivity of the FM layer. Recent studies on the exchange bias effect show that the interfacial spins produced by magnetically hard particles are responsible for the exchange bias effect and coercivity enhancement by virtue of their exchange coupling,[98] and that the interfacial spins produced by the magnetically soft phase (FeNi) do not contribute to the exchange bias.[99] The similarity between our system and the phase-separated system may lead us to suggest the same mechanism as being responsible for the observed exchange bias effects. Furthermore, according to a study on antiferromagnetic NiO

nanoparticles, it is predicted that a variety of reversal paths for the spin reversals may occur upon cycling the applied field due to the relatively weak coupling between the sublattices, thereby resulting in significantly large coercivities and loop shifts.[97–99] We could not rule out the possibility of the hysteresis loop shifts from the interfaces of small antiferromagnetic regions if the hysteresis shift was suppressed in the pure antiferromagnetic phase. In fact, because of our lack of knowledge about the volume fraction of the antiferromagnetic region as a function of the temperature in the sample, we are not yet going to come to a conclusive result for our $CuCrO_2$ compound. It requires finding the volume fraction of antiferromagnetic regions as a function of temperature on the samples annealed at various temperatures under atmospheric or high pressures in different atmospheres to change the surface morphology of the grains.

Resistivity

Electrical resistivity measurements of $CuCrO_2$ show a semiconducting behavior. At temperatures below 220 K, it becomes a perfect insulator. Figure 10 shows the resistivity as a function of temperature in the temperature range of 4–300 K. Currently, the four-point probe in our laboratory is unable to measure very high resistivity. Indeed, the sharp drop in resistivity bears a close resemblance to the superconducting behavior. However, our resistivity measurements indicate that the drop in resistivity arises entirely from the limited availability of high resistance. Recently, Tadee et al.[52] performed resistivity measurements on Fe-doped $CuCrO_2$ prepared using a self-combustion glycine nitrate process. Figure 11 is taken from this study. The most striking result to emerge from the resistivity data is that the resistivity clearly displays zero resistivity at temperatures below 118 K. The zero resistivity was taken as evidence of the superconductivity. However, there is no reliable evidence for superconductivity, although there is a significant drop in resistivity at lower temperatures.

Furthermore, Li et al.[101] have investigated the electrical, optical, and structural properties of amorphous $CuCrO_2$ films prepared by pulsed laser deposition using a nanocrystalline $CuCrO_2$ target synthesized by the sol–gel method. Interestingly, the resistivity of the thin film is three orders of magnitude smaller than that of the bulk $CuCrO_2$. They showed that unsaturated bonds and interstitial oxygen atoms

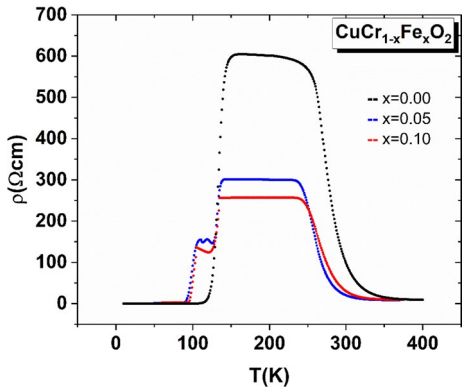

Fig. 11 Resistivity, ρ, as a function of temperature for sintered $CuCr_{1-x}Fe_xO_2$ (x = 0.00, 0.05, and 0.10) ceramics. The figure is reprinted from Ref. 100 (see Fig. 6 in Ref. 100).

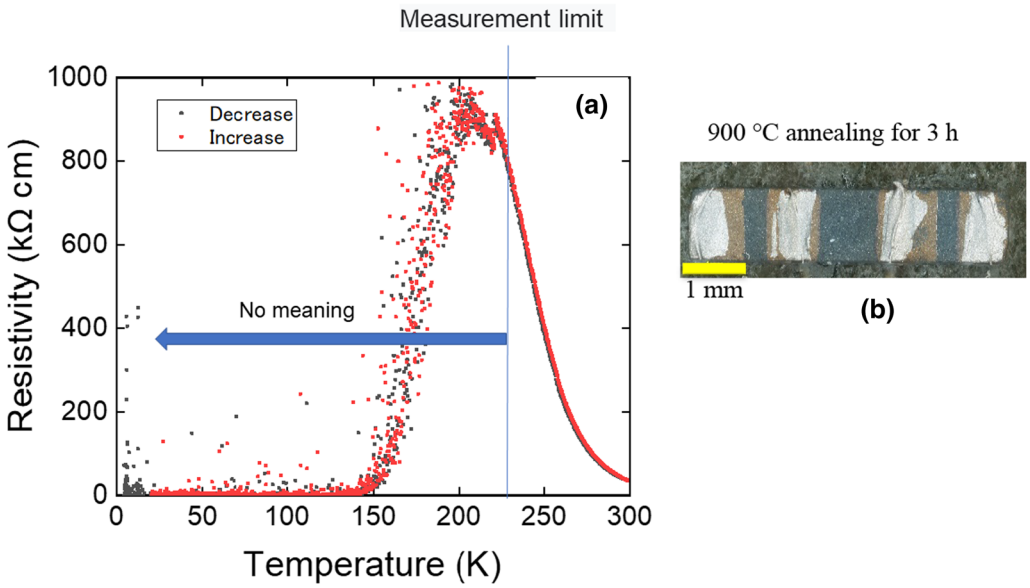

Fig. 10 Resistivity, ρ, as a function of temperature for the as-prepared sample of $CuCrO_2$ in (a) and a surface view of the rectangular shape bulk samples subjected to the HP acid treatment and surface polishing for the electrical resistivity measurements in (b).

have a major role in increasing the conductivity of the thin film. Lunca-Popa et al.[100] argued that the Cu vacancies chain defects are responsible for the high conductivity observed in this material. Akin et al.[102] demonstrated that Cu and O vacancies introduce holes in the lattice to enhance the conductivity. The intrinsic conduction of $CuCrO_2$ depends on defects, such as Cu vacancies and interstitial oxygen, as confirmed by Ngo et al.[103] Very recently, Liu et al.[104] showed that the reconfiguration of nanostructures on the surfaces of the nanoparticles of $CuCrO_2$ causes drastic changes in the structural and electronic properties.

In this study, we have also focused on the impurities' effects on the resistivity by annealing the sample under different thermal conditions, which may give a unique insight into the effect of the surface morphology on the resistivity. In the first stage, the resistivity and magnetization measurements were performed on the samples sintered at 900 °C/2 h (samples sintered at 900 °C are commonly used for measurements on delafossite systems). It is well known that higher sintering temperatures and shorter sintering times are required to achieve the desired degree of bonding between the powder particles in a powder compact. Then we tried sintering at 1000 °C, but the problem of weak grain boundaries was not solved, not leading to any noticeable changes in the resistivity results. However, when the sample was sintered under 4 GPa at 900 °C and 700 °C, Cu precipitation formed on the surface of the specimens. We also observed Cr_2O_3 and O on the surface determined by an x-ray diffraction pattern (see the supplementary material). The separation of some substitute Cu atoms is closely related to the bonding energy. Strongly bonding atoms show a low reactivity when exposed to the reactant air molecules. The weak binding energy of Cu inside grains may cause some different effects. For example, low-charge density due to low-energy bonding of Cu results in a tendency either towards an insulating state (as we observed a perfect insulator in the core of grains) or to the formation of magnetic states (some local short-range magnetic ordering occurring inside grains at low temperatures may be associated with weak bonding of the Cu atoms, as a possible case) or both states.

We assume that $CuCrO_2$ becomes a perfect insulator at temperatures below 220 K. The high-temperature paramagnetic resistivity can be analyzed by using different electrical conduction mechanisms that have often been used in describing the transport properties of similar delafossite compounds. In analogy to previous studies on transition metal oxides, we have performed a resistivity analysis by using the simple Arrhenius expression:

$$\rho = \rho_\infty \exp\left[\frac{E_a}{k_B T}\right] \tag{5}$$

The temperature dependence of the resistivity was fitted to the above equation. It is generally used to model activated behavior due to a band gap, E_a , or a mobility edge. It is assumed that ρ_∞ is a temperature-independent pre-factor, implying that neither the carrier mobility nor the carrier density changes with temperature.

The linear plot ln ρ versus 1000/T follows an Arrhenius-type law in a high T range above 260 K, as shown in Fig. 12a. The deviation from the linear behavior is presumably due to the thermal dependence of the pre-exponential factor or associated with the temperature dependence of broadband structures. In fact, the fitting yields reasonable values for the fitting parameters, $\rho_\infty \approx 23$ Ω-cm and $E_a \cong 350$ meV, exactly the same as previously reported by Majee et al.[105] However, the fitting after subtracting the temperature-independent residual resistivity term allows covering the whole measurement range, as shown in Fig. 12b, and provides many reasonable values for the fitting parameters, $\rho_\infty \approx 1.97$ Ω-cm

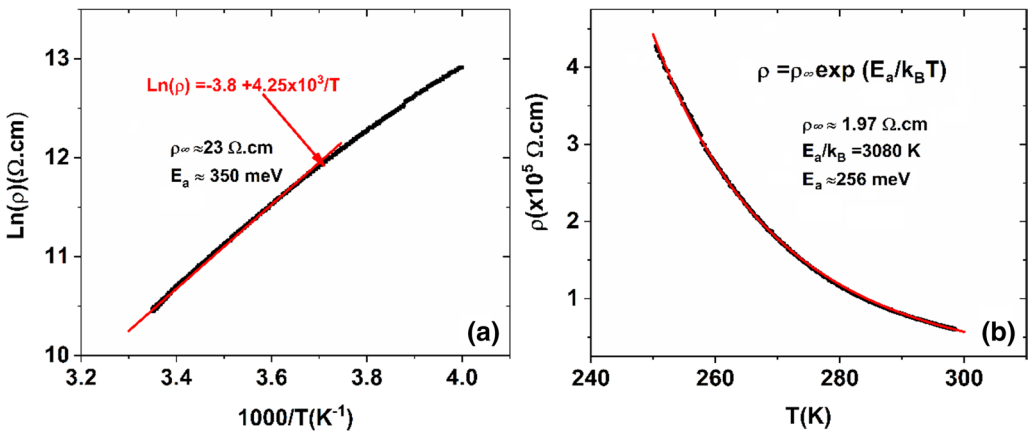

Fig. 12 Plots of (a) ln(ρ) versus 10^3 T^{-1} and (b) ρ versus T for $CuCrO_2$. The solid lines in (a) and (b) respectively are a fit of the simple Arrhenius expression, Eq. 5, to the data.

and $E_a \cong 256$ meV, consistent those previously obtained values.[106,107] In previous studies, the obtained activation energy, E_a, varies from one study to another between a few hundred meV and a few dozen meV.[108] It is commonly believed that the activation energy, E_a, decreases with increasing conductivity (either doped bulk sample or un-doped thin films). As argued above, the weak bonding energy of Cu implies that the constituted Cu atoms are bonded weakly to the lattice, thereby leading the localization to cause the formation of a mobility edge or to variable-range hopping between the localized states. Thus, it seems that the resistivity can be best described in terms of a general expression of Mott's variable range hopping (VRH)[28]:

$$\sigma = \sigma_0 \exp\left[\left(-\frac{T_0}{T}\right)^{\nu}\right] \tag{6}$$

where $\nu = 1/(\mathrm{d}+1)$, d is the dimensionality of the system. The present study confirms previous findings[109] and contributes additional evidence suggesting that localized Cu atoms have a predominant role in conductivity mechanisms. Ketir et al.[109] have argued that the conductivity of $CuCrO_2$ single crystal is highly anisotropic, being much greater perpendicular to the c-axis with a conductivity $\sigma_\perp$ of 3.36×10^{-5} Ω^{-1} cm^{-1}. $\sigma_\perp$ increases with increasing temperature and obeys an exponential law indicating semiconducting-like behavior. The authors have also demonstrated that the conductivity in $CuCrO_2$ can be described predominantly by small polaron hopping through mixed-valence states of $Cu^{+/2+}$ ions. It is noticed that the distance Cu^{+}-Cu^{+}, equal to the a-parameter, is larger than the interionic cation of the 3d overlap distance, which is a minimum distance required for the itinerant electron character. The Cu:3d electrons are strongly localized and manifested themselves by the large thermopower.[109] The presence of small polarons implies the existence of local lattice distortions, which also localize the charge carriers. The presence of local distortions[110] has been discussed in the previous sub-section. We assume that all requirements are satisfied for this fitting. We performed the resistivity analysis in terms of small polaron hopping conduction where the conductivity can be expressed by:

$$\sigma = \frac{\sigma_0}{T} \exp\left(-E_a/k_B T\right), \tag{7}$$

where E_a is the activation energy, and σ_0 is the pre-exponential factor. In this case, the small polaron has low mobility and behaves like a heavy particle with a finite mean-free path (l), such that the quantity (k_F l) becomes less than unity, of being the wave vector and l the mean-free path, according to the Ioffe–Regel criteria.

Figure 13 shows the plots of ln(σT) versus T^{-1} for the polycrystalline $CuCrO_2$. The linear fit yields the values of E_a indicated in the figure, which are consistent with those

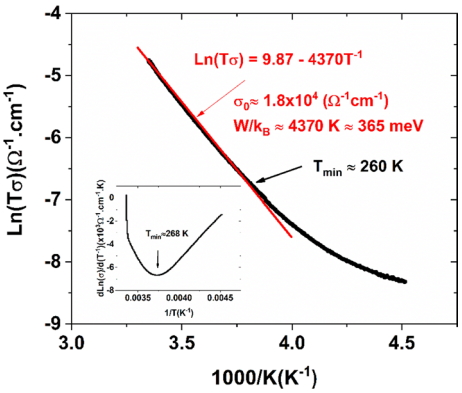

Fig. 13 Plot $Ln(\sigma T)$ versus 10^3 T^{-1} T for $CuCrO_2$. The *solid line* is the fit of the polaron hopping conduction expression in Eq. 7. Note that a clear deviation is apparent around 260 K, at which d [$Ln\sigma T$/d(T^{-1})] gives a maximum.

reported for other transition metal oxides. However, the fitting is limited to temperatures below 265 K. It is also noted that the derivative d(σ)/d(1/T) behaves in a non-monotonic behavior with temperature. On the other hand, it is generally predicted that the conduction mechanism changes from the thermally activated small polaron hopping to VRH conduction with decreasing temperature. This crossover was previously observed in $CuCrO_2$[111] and $CuCr_{0.95}Mg_{0.05}O_2$ thin film. Okuda et al.[106] have pointed out the crossover from thermal activation to VRH occurs around the Curie–Weiss temperature θ_{CW} (for $CuCrO_2$, it is about 300 K), leading to suggestions that the conductivity is coupled with the AF correlation. One of the most obvious findings to emerge from the resistivity study is that the fitting ($T > 300$ K) based on the VRH mechanism confirms this assertion, as given below. A similar electrical mechanism can be found in other Cu-based delafossite structure materials.

The conductivity of $CuCrO_2$ has a mainly 2D character since its conductivity is highly anisotropic, as mentioned above. A value of $\nu = 1/3$ is predicted for VRH transport in 2D. Therefore, the general Mott's expression reduces to:

$$\sigma = \sigma_\infty \exp\left[\left(-\frac{T_0}{T}\right)^{1/3}\right], \tag{8}$$

It seems most appropriate to describe the resistivity data in a wide temperature range, which means that the carriers are localized by random potential fluctuations hopping. According to this model, thermally activated electrons move from site to site by the same thermally activated tunneling process (hopping).

Figure 14 shows the $\sigma(T)$ versus T plot with the model-fitted curve. The quality of the fitting indicates that the model is a good fit for the data. The values of the best-fitting parameters are $\sigma_0 = 1.385 \times 10^{16}$ Ω^{-1} cm^{-1}, $T_0 = 3.05 \times 10^7$ K,

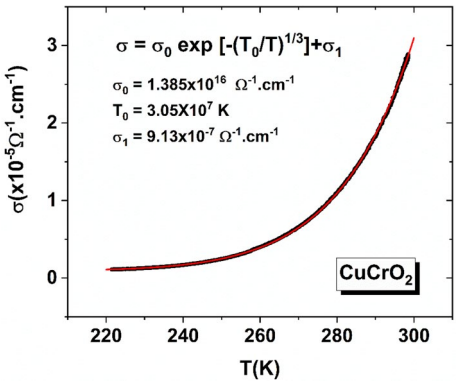

Fig. 14 Conductivity, σ, of the $CuCrO_2$ sample as a function of temperature, T. The solid line is a fit of the VRH model ($T^{-1/4}$ behavior) to the data, using Eq. 8 with an additional temperature-independent term, corresponding to the resistivity of the sample in the pure insulating phase.

$\sigma_1 = 9.13 \times 10^{-7}\ \Omega^{-1}\ \text{cm.}^{-1}$. The value of T_0 is smaller by one order of magnitude than that reported by Majee et al.[105] However, they assumed that the conductivity in $CuCrO_2$ has a 3D character, whereas they should have a 2D form for the resistivity, in accordance with the lack of multiferroicity at higher temperatures.[33] The conductivity increases with temperature from the completely pure insulator state with the conductivity, σ_1 , to the conductivity, $\sigma(T)$, at the measuring temperature, T. Here, the temperature scale T_0 is related to the localization length ξ by Ref. 112:

$$k_B T_0 = \frac{24}{\pi N(E_F)\xi^3}, \tag{9}$$

$N(E_F)$ denotes the density of states at the Fermi level. From Eq. 9, and using $T_0 = 3.5 \times 10^7$ K with the localization length estimated as $\xi \approx 0.25$ nm (it should be less than the distance Cu^+-Cu^+, a = 0.297 nm), we obtain the density of states at the Fermi energy to be $N(E_F) \sim 6 \times 10^{20}\ \text{eV}^{-1}\ \text{cm}^{-1}$, which lies in the region predicted for doped semiconductors (10^{18}–$10^{20}\ \text{eV}^{-1}\ \text{cm}^{-3}$).[112]

Conclusions

Magnetic and electrical properties of polycrystalline $CuCrO_2$ prepared by usual solid-state reaction crystalized with the space group have been studied as a function of the field (up to $H = 9$ T) and the temperature (in the range of 10–400 K). We have observed a transition from a high-temperature paramagnetic phase to an inhomogeneous mixed phase with short-range antiferromagnetic ordering in the intermediate temperature range. As the temperature decreases, it is followed by a magnetic phase transition to an antiferromagnetic state at about 24 K, manifesting itself as a stair-like drop in the magnetization curve. The short-range antiferromagnetic correlations act as weak ferromagnets in the applied field. These order regions are suppressed by magnetic fields exceeding 0.5 T, evidenced by the positive deviation of $\chi^{-1}(T)$ from Curie–Weiss at $H = 9$ T. Consequently, we conclude that interstitial oxygen (e.g., its related defects) plays a crucial role in causing local distortion on the CrO_6 tetrahedral, which gives rise to the enhancement of magnetization.

There are a few subtle points that are worth emphasizing in the magnetically inhomogeneous mixed phase. Based on the magnetic analyses using a modified Langevin function, it has been shown that the nano-size antiferromagnetic order region behaves as a weak ferromagnet. Thermo-induced moments are induced inside the grains due to weak antiferromagnetically coupled sublattices and become dominant over uncompensated spins. To understand the nature of the inhomogeneously magnetic ordered state, we have used Griffith's phase approach. However, the analyses do not provide a favorable result to support the presence of Griffith's phase.

More interestingly, the magnetization data show negative magnetization in the zero-field-cooling $M_{ZFC}(T)$ curve below about 140 K, where the magnetization curve splits into $M_{FC}(T)$ and $M_{ZFC}(T)$ branches. The negative magnetization is explained by considering the paramagnetic moment of Cr ions under the influence of a self-induced negative internal field due to lattice distortions. Two possible scenarios have been suggested for the origin of its driving force: spin–lattice coupling in such a frustrating system causes inherently to the internal negative field, or the exchange magneto-striction mechanism may become solely responsible for that field. The reason behind this is the magnetoelastic stress occurring on triangular Cr layers through the Cu-O-Cu coupling (interlayers coupling).

In the presence of external magnetic fields, the system displays the exchange bias phenomenon. We observed exchange bias effects at T = 10 K and 50 K below and above the Néel temperature, T_N (~ 24 K) in both the horizontal (H_{uni}) and vertical directions (ΔM_E) in the FC case for $H_{cool} = 0.5$ T. The hysteresis loop shifts from the origin along both the field axis and the magnetization axes with a temperature, T, and cooling field, H_{cool} , dependence. Both exchange bias effects are suppressed at $H_{cool} = 9$ T, but with significant coercivity enhancements. Our results demonstrate that the exchange-biased phenomenon originates at the interfacial exchange interactions on the grain boundaries. As a result, the origin of the exchange bias effects has been attributed to the interfacial exchange interactions between the magnetically disordered (spin-glass-like) grain boundary and the antiferromagnetically ordered regions inside the grains.

Finally, resistivity measurements were performed in samples with different thermal treatment conditions. It is

concluded that the resistivity dropping to zero does not originate from superconductivity, as previously suggested by Tadee et al.,[52] but the semiconductor $CuCrO_2$ behaves as an ideal antiferromagnetic insulator at lower temperatures. The resistivity above 220 K has been described as well based on the variable range hopping conduction model, first suggested by Mott.

Supplementary Information The online version contains supplementary material available at https://doi.org/10.1007/s11664-023-10423-9.

Acknowledgments This research did not receive any specific grant from funding agencies in the public, commercial, or not-for-profit sectors.

Conflict of interest The authors declare that they have no conflict of interest.

References

1. S. Seki, Y. Yamasaki, Y. Shiomi, S. Iguchi, Y. Onose, and Y. Tokura, Impurity-doping-induced ferroelectricity in the frustrated antiferromagnet $CuFeO_2$. *Phys. Rev. B* 75, 100403(R) (2007).
2. F. Ye, J.A. Fernandez-Baca, R.S. Fishman, Y. Ren, H.J. Kang, Y. Qiu, and T. Kimura, Magnetic interactions in the geometrically frustrated triangular lattice antiferromagnet $CuFeO_2$. *Phys. Rev. Lett.* 99, 157201 (2007).
3. Y. Ajiro, T. Asano, T. Takagi, M. Mekata, H.A. Katori, and T. Goto, High-field magnetization process in the triangular lattice antiferromagnet $CuFeO_2$ up to 100 T. *Phys. B* 201, 71 (1994).
4. T. Kimura, J.C. Lashley, and A.P. Ramirez, Inversion-symmetry breaking in the noncollinear magnetic phase of the triangular-lattice antiferromagnet $CuFeO_2$. *Phys. Rev. B* 73, 220401 (2006).
5. H. Mitamura, S. Mitsuda, S. Kanetsuki, H.A. Katori, T. Sakakibara, and K. Kindo, Dielectric polarization measurements on the antiferromagnetic triangular lattice system $CuFeO_2$ in pulsed high magnetic fields. *J. Phys. Soc. Jpn.* 76, 094709 (2007).
6. O.A. Petrenko, G. Balakrishnan, M.R. Lees, D.M.K. Paul, and A. Hoser, High-magnetic-field behavior of the triangular-lattice antiferromagnet $CuFeO_2$. *Phys. Rev. B* 62, 13 (2000).
7. N.O. Moreno, C. Israel, P.G. Pagliuso, A.J. Garcia-Adeva, C. Rettori, J.L. Sarrao, J.D. Thompson, and S.B. Oseroff, Magnetic properties of the frustrated antiferromagnet $LiCrO_2$. *J. Magn. Magn. Mater.* 272, e1023–e1024 (2004).
8. K. Hirakawa, H. Kadowaki, and K. Ubukoshi, Experimental studies of triangular lattice antiferromagnets with $S = 1/2$: $NaTiO_2$ and $LiNiO_2$. *J. Phys. Soc. Jpn.* 54, 3526–3536 (1985).
9. H. Kawazoe, M. Yasukawa, H. Hyodo, M. Kurita, H. Yanagi, and H. Hosono, *p*-type electrical conduction in transparent thin films of $CuAlO_2$. *Nature (London)* 389, 939 (1997).
10. A. Stadler, Transparent conducting oxides—an up-to-date overview. *Materials (Basels)* 5(4), 661–683 (2012).
11. A.N. Banerjee and K. Chattopadhyay, Recent developments in the emerging field of crystalline *p*-type transparent conducting oxide thin films. *Prog. Cryst. Growth Charact.* 50, 52 (2005).
12. A.P. Ramirez, *Handbook of Magnetic Materials* (Amsterdam: Elsevier, 2001).
13. P. Schiffer and A.P. Ramirez, Recent experimental progress in the study of geometrical magnetic frustration. *Comments J. Condens. Matter Phys.* 18, 21 (1996).
14. A.P. Ramirez, Strongly geometrically frustrated magnets. *Annu. Rev. Mater. Sci.* 24, 453 (1994).
15. M.J. Harris and M.P. Zinkin, Magnetic structures of highly frustrated pyrochlores. *Mod. Phys. Lett. B* 10, 417 (1996).
16. T. Kimura, T. Goto, H. Shintani, K. Ishizaka, T. Arima, and Y. Tokura, Magnetic control of ferroelectric polarization. *Nature* 426, 55 (2003).
17. T. Kimura, J.C. Lashley, and A.P. Ramirez, Inversion-symmetry breaking in the noncollinear magnetic phase of the triangular-lattice antiferromagnet $CuFeO_2$. *Phys. Rev. B* 73, 220401(R) (2006).
18. S.W. Cheong and M. Mostovoy, Multiferroics: a magnetic twist for ferroelectricity. *Nat. Mater.* 6, 13 (2007).
19. Y.A. Sakhratov, J.J. Kweon, E.S. Choi, H.D. Zhou, L.E. Svistov, and A.P. Reyes, Search for a nematic phase in the quasi-two-dimensional antiferromagnet $CuCrO_2$ by NMR in an electric field. *Phys. Rev. B* 97, 094409 (2018).
20. K. Kimura, H. Nakamura, S. Kimura, M. Hagiwara, and T. Kimura, Tuning ferroelectric polarization reversal by electric and magnetic fields in $CuCrO_2$. *Phys. Rev. Lett.* 103, 107201 (2009).
21. H. Yamaguchi, S. Ohtomo, S. Kimura, M. Hagiwara, K. Kimura, T. Kimura, T. Okuda, and K. Kindo, Spiral-plane flop probed by ESR in the multiferroic triangular-lattice antiferromagnet $CuCrO_2$. *Phys. Rev. B* 81, 033104 (2010).
22. R.S. Fishman, Phase diagram of $CuCrO_2$ in a magnetic field. *J. Phys. Condens. Matter* 23, 366002 (2011).
23. A. Miyata, O. Portugall, D. Nakamura, K. Ohgushi, and S. Takeyama, Ultrahigh magnetic field phases in the frustrated triangular-lattice magnet $CuCrO_2$. *Phys. Rev. B* 96, 180401(R) (2017).
24. D. Ledue, W.L. Ndzamba, R. Patte, and A. Albaalbaky, Magnetic field induced phases in $CuCrO_2$: Monte Carlo and analytical investigations. *Phys. Rev. B* 103, 094401 (2021).
25. O. Crottaz, F. Kubel, and H.J. Schmid, Preparation of trigonal and hexagonal cuprous chromite and phase transition study based on single crystal structure data. *Solid State Chem.* 122, 247 (1996).
26. H. Kadowaki, H. Kikuchi, and Y. Ajiro, Neutron powder diffraction study of the two-dimensional triangular lattice antiferromagnet $CuCrO_2$. *J. Phys. Condens. Matter* 2, 4485–4493 (1990).
27. K. Kimura, H. Nakamura, K. Ohgushi, and T. Kimura, Magnetoelectric control of spin-chiral ferroelectric domains in a triangular lattice antiferromagnet. *Phys. Rev. B* 78, 140401(R) (2008).
28. N.F. Mott, Conduction in glasses containing transition metal ions. *J. Non-Cryst. Solids* 1, 1 (1968).
29. R. Nagarajan, A. Draeseke, A. Sleight, and J. Tate, *p*-type conductivity in $CuCr_{1-x}Mg_xO_2CuCr_{1-x}Mg_xO_2$ films and powders. *J. Appl. Phys.* 89(12), 8022–8025 (2001).
30. T. Okuda, T. Onoe, Y. Beppu, N. Terada, T. Doi, S. Miyasaka, and Y. Tokura, Magnetic and transport properties of delafossite oxides $CuCr_{1-x}(Mg, Ca)_xO_2$. *J. Magn. Magn. Mater.* 310(2), 890–892 (2007).
31. D.V. Hoang, T.A.K. Le, A. Tuan, T. Pham, H. Kieu, T. Ta, N.K. Pham, T.H. Nguyen, H.T. Lai, D.C. Truong, N.V. Le, C.T. Huynh, S.C.H. Park, S. Song, T. Mori, V.C. Tran, and T.B. Phan, The roles of interstitial oxygen and phase compositions on the thermoelectric properties $CuCr_{0.85}Mg_{0.15}O$, delafossite material. *J. Alloys Compd.* 867, 158995 (2021).
32. X.R. Li, M.J. Han, P. Chang, Z.G. Hu, Y.W. Li, Z.Q. Zhu, and J.H. Chu, Temperature dependence of terahertz optical characteristics and carriertransport dynamics in *p*-type transparent conductive $CuCr_{1-x}Mg_xO_2$ semiconductor films. *Appl. Phys. Lett.* 104(1), 012103 (2014).
33. T. Okuda, N. Jufuku, S. Hidaka, and N. Terada, Magnetic, transport, and thermoelectric properties of the delafossite oxides $CuCr_{1-x}Mg_xO_2$ ($0 \leqslant x \leqslant 004$). *Phys. Rev. B* 72, 144403 (2005).

34. T. Okuda, S. Oozono, T. Kihara, and M. Tokunaga, Thermal transport and magnetotransport properties of $CuCr_{1-x}Mg_xO_2$ with a spin-3/2 antiferromagnetic triangular lattice. *J. Phys. Soc. Jpn.* 82, 014706 (2013).
35. L. Renwen, Z. Qu, W. Tong, and Y. Zhang, Spin dynamics in triangular lattice antiferromagnets $CuCr_{1-x}Mg_xO_2$. *EPL* 93, 37004 (2011).
36. T. Okuda, Y. Beppu, Y. Fujii, T. Kishimoto, K. Uto, T. Onoe, N. Jufuku, S. Hidaka, N. Terada, and S. Miyasaka, Hole-doping effect on the magnetic state of delafossite oxide $CuCrO_2$, in *Journal of Physics: Conference Series* (2009), p. 042157.
37. M. Amami, F. Jlaiel, P. Strobel, and A.B. Salah, Synthesis structural and magnetic studies of the $CuCr_{1-x}Rh_xO_2$ delafossite solid solution with $0 \leq x \leq 0.2$. *Mater. Res. Bull.* 46, 1729–1733 (2011).
38. F. Jlaiel, M. Amami, N. Boudjada, P. Strobel, and A.B. Salah, Metal transition doping effect on the structural and physical properties of delafossite-type oxide $CuCrO_2$. *J. Alloys Compd.* 509, 7784–7788 (2011).
39. T. Elkhouni, M. Amami, P. Strobel, and A.B. Salah, Evidence of development of new spin orders benefiting to enhance magnetic properties in Co^{2+}-doped delafossite-type oxide $CuCrO_2$. *J. Supercond. Nov. Magn.* 28, 1–8 (2015).
40. T. Elkhouni, M. Amami, C.V. Colin, P. Strobel, and A.B. Salah, Synthesis, structural and magnetic studies of the $CuCr_{1-x}Co_xO_2$ delafossite oxide. *J. Magn. Magn. Mater.* 330, 101–105 (2013).
41. A.A. Shaha, A. Parveena, P.A. Alvib, and A. Azam, Low temperature synthesis and effect of Co doping on structural, optical and dielectric properties of $CuCrO_2$ hexagonal nanoplates. *Ceram. Int.* 46, 19827–19834 (2020).
42. M. Amami, C.V. Colin, P. Strobel, and A.B. Salah, Al-doping effect on the structural and physical properties of delafossite-type oxide $CuCrO_2$. *Physica B* 406, 2182–2185 (2011).
43. F. Jlaiel, M. Amami, P. Strobel, and A.B. Salah, Non-magnetic impurity doping effect on the magnetic state of *p*-type Al-doped delafossite oxide $CuCrO_2$. *Cent. Eur. J. Chem.* 9(5), 953–958 (2011).
44. D.O. Scanlon, A. Walsh, B.J. Morgan, and G.W. Watson, Effect of Cr substitution on the electronic structure of $CuAl_{1-x}Cr_xO_2$. *Phys. Rev. B* 79, 035101 (2009).
45. L. Shijun, L. Li, K.F. Wang, S.Z. Li, X.W. Dong, Z.B. Yan, and J.M. Liu, Enhanced magnetic and ferroelectric properties of multiferroic $CuCrO_2$ by Ni-doping. *Thin Solid Films* 518, e50–e53 (2010).
46. S.J. Luo, K.F. Wang, S.Z. Li, X.W. Dong, Z.B. Yan, H.L. Cai, and J.M. Liu, Enhanced ferromagnetism and ferroelectricity in multiferroic $CuCr_{1-x}Ni_xO_2$. *Appl. Phys. Lett.* 94, 172504 (2009).
47. D. Li, X.D. Fang, W.W. Dong, Z.H. Deng, R.H. Tao, S. Zhou, J.M. Wang, T. Wang, Y.P. Zhao, and X.B. Zhu, Magnetic and electrical properties of *p*-type Mn-doped $CuCrO_2$ semiconductors. *J. Phys. D Appl. Phys.* 42, 055009 (2009).
48. Y.F. Wang, Y.J. Gu, T. Wang, and W.Z. Shi, Magnetic, optical and electrical properties of Mn-doped $CuCrO_2$ thin films prepared by chemical solution deposition method. *J. Sol-Gel Sci. Technol.* 59, 222–227 (2011).
49. L. Xie, H.G. Zhang, H.L. Huang, Y.L. Lu, J.Q. Yu, M.H. Li, X.Q. Tang, and C. Wang, Coexistence of magnetization reversal and exchange bias in Mn-substituted $CuCrO_2$. *J. Alloys Compd.* 772, 703–709 (2019).
50. K.K. Shukla, A. Pal, A. Singh, R. Singh, J. Saha, A.K. Sinha, A.K. Ghosh, S. Patnaik, A.M. Awasthi, and S. Chatterjee, Hidden transition in multiferroic and magnetodielectric $CuCrO_2$ evidenced by ac-susceptibility. *EPL* 118, 27008 (2017).
51. C. Gao, F. Lin, X. Zhou, W. Shi, and A. Liu, Fe concentration dependences of microstructure and magnetic properties for Cu $(Cr_{1-x}Fe_x)$ O_2 ceramics. *J. Alloys Compd.* 565, 154–158 (2013).
52. C. Taddee, T. Kamwanna, and V. Amornkitbamrung, Characterization of transparent superconductivity Fe-doped $CuCrO_2$ delafossite oxide. *Appl. Surf. Sci.* 380, 237–242 (2016).
53. M.K. Majee, P.A. Bhobe, and A.K. Nigam, Griffiths phase in antiferromagnetic $CuCr_{0.95}Ti_{0.05}O_2$. *J. Magn. Magn. Mater.* 485, 112–117 (2019).
54. M.K. Majee, P.A. Bhobe, and A.K. Nigam, Magnetic properties of delafossite oxide: $CuCr_{1-x}Ti_xO_2$, in *AIP Conference Proceedings* (2016) p. 130022.
55. T. Elkhouni, M. Amami, P. Strobel, and A. Ben Salah, Structural, raman spectroscopy, and magnetic ordering in new delafossite-type oxide $CuCr_{1-x}Ti_xO_2$ $(0 \leq x \leq 0.1)$. *J. Supercond. Nov. Magn.* 26, 2795–2802 (2013).
56. M.K. Majee, P.A. Bhobe, U.P. Deshpande, and A.K. Nigam, Local crystal structure and physical properties change of *p*-type transparent conducting oxide: $CuCrO_2$ upon Ti-substitution. *J. Appl. Phys.* 122, 225111 (2017).
57. L. Renwen and Z.Q.Y. Zhang, Slight Ti-doping-induced strong time-dependent electrical transport behavior in $CuCr_{1-x}Ti_xO_2$. *J. Am. Ceram. Soc.* 98(8), 2503–2507 (2015).
58. H.Y. Chen and C.C. Yang, Transparent *p*-type Zn-doped $CuCrO_2$ films by sol–gel processing. *Surf. Coat. Technol.* 231, 277–280 (2013).
59. T. Elkhouni, M. Amami, P. Strobel, and A.B. Salah, Structural and magnetic properties of substituted delafossite-type oxides $CuCr_{1-x}Sc_xO_2$. *World J. Condens. Matter Phys.* 3, 1–8 (2013).
60. K. Singh, A. Maignan, C. Simon, S. Kumar, C. Martin, O. Lebedev, S. Turner, and G. van Tendeloo, Magnetodielectric $CuCr_{0.5}V_{0.5}O_2$: an example of a magnetic and dielectric multiglass. *J. Phys. Condens. Matter* 24, 226002 (2012).
61. S. Kumar, K. Singh, M. Miclau, C. Simon, C. Martin, and A. Maignan, From spin induced ferroelectricity to spin and dipolar glass in a triangular lattice: the $CuCr_{1-x}V_xO_2$ $(0 \leq x \leq 0.5)$ delafossite. *J. Solid State Chem.* 203, 37 (2013).
62. T. Okuda, K. Uto, S. Seki, Y. Onose, Y. Tokura, R. Kajimoto, and M. Matsuda, Effect of spin dilution on the magnetic state of delafossite $CuCrO_2$ with an $S = 3/2$ antiferromagnetic triangular sublattice. *J. Phys. Soc. Jpn.* 80, 014711 (2011).
63. Z.R. Yan, M.H. Qin, S. Dong, M. Zeng, X.B. Lu, X.S. Gao, and J.M. Liu, Spin glass state and enhanced spiral phase in doped delafossite oxide $CuCrO_2$. *Phys. Rev. B* 94, 024410 (2016).
64. T. Okuda, R. Kazimoto, M. Okawa, and T. Saitoh, Effect of hole-doping and disorder on the magnetic states of delaossite $CuCrO_2$ having a spin-3/3 abtiferromagnetic triangular sublattice. *Int. J. Mod. Phys. B* 27, 43 (2013).
65. Z. Bai, S.C. Chen, S.S. Lin, Q. Shi, Y.B. Lu, S.M. Song, and H. Sun, Review in optoelectronic properties of *p*-type $CuCrO_2$ transparent conductive films. *Surf. Interfaces.* 22, 100824 (2021).
66. A.H. Cooke, D.M. Martin, and M.R. Wells, Magnetic interactions in gadolinium orthochromite, $GdCrO_3$. *J. Phys. C Solid State Phys.* 7, 3133 (1974).
67. K. Yoshii, Magnetic properties of perovskite $GdCrO_3$. *J. Solid State Chem.* 159, 204–208 (2001).
68. K. Yoshii, Positive exchange bias from magnetization reversal in $La_{1-x}Pr_xCrO_3$ (x similar to 0.7–0.85). *App. Phys. Lett.* 99, 142501 (2011).
69. D. Fu, Y. Liu, H. Zhang, L. Xie, and B. Li, The evolution of magnetization switching of $LuCrO_3$ by the effect of Mn doping. *J. Alloys Compd.* 735, 1052e–11062 (2018).
70. T. Bora and S. Ravi, Sign reversal of magnetization and exchange bias field in $LaCr_{0.85}Mn_{0.15}O_3$. *J. Appl. Phys.* 114, 183902 (2013).
71. T. Bora and S. Ravi, Bipolar switching of magnetization and tunable exchange bias in $NdCr_{1-x}Mn_xO_3$ (x=0.0–0.30). *J. Appl. Phys.* 116, 063901 (2014).

72. T. Bora and S. Ravi, Negative magnetization and the tunable exchange bias field in $LaCr_{0.8}Mn_{0.2}O_3$. *J. Magn. Magn. Mater.* 358–359, 208–211 (2014).
73. S. Huang, R. Jiang, J.Y. Wei, J. Yang, J.Y. Ge, D.X. Yang, and D.X. Huo, The negative magnetization and dielectric relaxation in $(La_{0.3}Pr_{0.7})_{1-x}Ca_xCrO_3$ ceramics. *Ceram. Int.* 46, 22221–22229 (2020).
74. C.L. Li, T.Y. Yan, G.O. Barasa, Y.H. Li, R. Zhang, Q.S. Fu, X.H. Chen, and S.L. Yuan, Negative magnetization and exchange bias effect in Fe-doped $CoCr_2O_4$. *Ceram. Int.* 44, 15446–15452 (2018).
75. Q.S. Fu, X.H. Chen, C. Chakrabarti, C.L. Li, J. Zheng, P.J. Wang, H.X. Yin, Y. Qiu, B. Meng, and S.L. Yuan, Negative magnetization, complex magnetic ordering and applications of Cr-doped Co_2TiO_4. *Phys. Chem. Chem. Phys.* 22, 7058–7064 (2020).
76. S.N. Sofronova, N.V. Kazak, E.V. Eremin, E.M. Moshkina, A.V. Chernyshov, and A.F. Bovina, Magnetization reversal and sign reversal exchange bias field in polycrystalline $Ni_{5.33}Ta_{0.67}B_2O_{10}$. *J. Alloys Compd.* 864, 158200 (2021).
77. M. Tripathi, T. Chatterji, H.E. Fischer, R. Raghunathan, S. Majumder, R.J. Choudhary, and D.M. Phase, Role of local short-scale correlations in the mechanism of negative magnetization. *Phys. Rev. B* 99, 014422 (2019).
78. A. Kumar and S.M. Yusuf, The phenomenon of negative magnetization and its implications. *Phys. Rep.* 556, 1–34 (2015).
79. K. Kimura, T. Otani, H. Nakaramu, Y. Wakabayashi, and T. Kimura, Lattice distortion coupled with magnetic ordering in a triangular lattice antiferromagnet $CuCrO_2$. *J. Phys. Soc. Jpn.* 78, 113710 (2009).
80. A.E. Berkowitz and K. Takano, Exchange anisotropy—a review. *J. Magn. Magn. Mater.* 200, 552 (1999).
81. S. Morup and C. Frandsen, Thermo-induced magnetization in nanoparticles of antiferromagnetic materials. *Phys. Rev. Lett.* 92, 217201 (2004).
82. M.S. Seehra, V.S. Babu, A. Manivannan, and J.W. Lynn, Neutron scattering and magnetic studies of ferrihydrite nanoparticles. *Phys. Rev. B* 61, 3513 (2000).
83. S. Morup, D.E. Madsen, C. Frandsen, C.R. Bahl, and M.F. Hansen, Experimental and theoretical studies of nanoparticles of antiferromagnetic materials. *J. Phys. Condens. Matter* 19, 213202 (2007).
84. T. Moriya, Anisotropic superexchange interaction and weak ferromagnetism. *Phys. Rev.* 120, 91 (1960).
85. H.J. Zhao, J.I. Niguez, X.M. Chen, and L. Bellaiche, Origin of the magnetization and compensation temperature in rare-earth orthoferrites and orthochromates. *Phys. Rev. B* 93, 014417 (2016).
86. Y. Oner, C. Boyraz, H. Hiramatsu, T. Katase, and H. Hosono, Coexistence of magnetism and superconductivity in thin films of the Fe-based superconductor $Ba_{1-x}La_xFe_2As_2$. *J. Phys. Condens. Matter* 32(48), 485804 (2020).
87. Y. Oner and M. Guillot, Magnetic disordered in Ti doped $ErCo_2$ alloys: Griffiths-like behavior. *J. Magn. Magn. Mater.* 324(20), 3313–3322 (2012).
88. M. Zou, V.K. Pecharsky, K.A. Gschneidner Jr., D.L. Schlagel, and T.A. Lograsso, Magnetic phase transitions and ferromagnetic short-range correlations in single-crystal $Tb_5Si_{2.2}Ge_{1.8}$. *Phys. Rev. B* 78, 014435 (2008).
89. Z.W. Ouyang, V.K. Pecharsky, K.A. Gschneidner Jr., D.L. Schlagel, and T.A. Lograsso, Short-range anisotropic ferromagnetic correlations in the paramagnetic and antiferromagnetic phases of Gd_5Ge. *Phys. Rev. B* 74, 094404 (2006).
90. M.K. Majee, P.A. Bhobe, and A.K. Nigam, Griffith's phase in antiferromagnetic $CuCr_{0.95}Ti_{0.05}O_2$. *J. Magn. Magn. Mater.* 485, 112–117 (2019).
91. J. Nogues and I.K. Schuller, Exchange bias. *J. Magn. Magn. Mater.* 192, 203 (1999).
92. R.K. Zheng, G.H. Wen, K.K. Fung, and X.X. Zhang, Giant exchange bias and the vertical shifts of hysteresis loops in Υ-Fe_2O_3-coated Fe nanoparticles. *J. Appl. Phys.* 95, 5244 (2004).
93. H. Khurshid, W. Li, M.H. Phan, P. Mukherjee, G.C. Hadjipanayis, and H. Srikanth, Surface spin disorder and exchange-bias in hollow maghemite nanoparticles. *Appl. Phys. Lett.* 101, 022403 (2012).
94. L. Sun, P.C. Searson, and C.L. Chien, Asymmetrical hysteresis in exchange-biased multilayers with out-of-plane applied fields. *Phys. Rev. B* 71, 012417 (2005).
95. M. Zheng, X. Li, W. Xiao, W. Wang, and H. Ni, Oxygen deficiency and cooling field driven vertical hysteretic shift in epitaxial $SrRuO_3/SrTiO_3$ heterostructures. *Appl. Phys. Lett.* 111, 152405 (2017).
96. Y. Tang, Y. Sun, and Z. Cheng, Exchange bias associated with phase separation in the perovskite cobaltite $La_{1-x}Sr_xCoO_3$. *Phys. Rev. B* 73, 174419 (2006).
97. K.O. Grady, L.E. Fernandez, and G. Vallejo-Fernandez, A new paradigm for exchange bias in polycrystalline thin films. *J. Magn. Magn. Mater.* 322, 883–899 (2010).
98. A.E. Berkowitz, J.-I. Hong, S.K. McCall, E. Shipton, K.T. Chan, T. Leo, and D.J. Smith, Refining the exchange anisotropy paradigm: magnetic and microstructural heterogeneity at the permalloy-CoO interface. *Phys. Rev. B* 81, 134404 (2010).
99. A. Mannan, P. Adie, C.H. Marrows, D. Greig, B.J. Hickey, and R.L. Stamps, Exchange bias using a spin glass. *Nat. Mater.* 6, 70–75 (2007).
100. P.L. Popa, J. Afonso, P. Grysan, J. Crêpellière, R. Leturcq, and D. Lenoble, Tuning the electrical properties of the *P*-type transparent conducting oxide $Cu_{1-x}Cr_{1+x}O_2$ by controlled annealing. *Sci. Rep.* 8, 7216 (2018).
101. D. Li, X. Fang, Z. Deng, S. Zhou, R. Tao, W. Dong, T. Wang, Y. Zhao, G. Meng, and X. Zhu, Electrical, optical and structural properties of $CuCrO_2$ films prepared by pulsed laser deposition. *J. Phys. D Appl. Phys.* 40, 4910–4915 (2007).
102. S. Akin, Y. Liu, M.I. Dar, S.M. Zakeeruddin, M. Gratzel, S. Turand, and S. Sonmezoglu, Hydrothermally processed $CuCrO_2$ nanoparticles as an inorganic hole transporting material for low-cost perovskite solar cells with superior stability. *J. Mater. Chem. A* 6, 20327 (2018).
103. T.N.M. Ngo, T.T.M. Palstra, and G.R. Blake, Crystallite Size dependence of thermoelectric performance of $CuCrO_2$. *RSC Adv.* 6, 91171–91178 (2016).
104. H. Liu, W. Zhu, X. Ding, Y. Huang, and M. Bo, Abnormal deviation of temperature−resistivity correlation for nanostructured delafossite $CuCrO_2$ due to local reconfiguration. *J. Phys. Chem. C* 124, 28555–28561 (2020).
105. M.K. Majee and P.A. Bhobe, Correlation of local crystal structural and physical properties of the delafossite $CuCr_{1-x}Fe_xO_2$ ($0 \leq x \leq 1$) series. *Inorg. Chem.* 59, 6790–6799 (2020).
106. T. Okuda and R. Kajimoto, Effects of hole-doping and disorder on the magnetic states of delafossite $CuCrO_2$ having a spin−3/2 antiferromagnetic triangular sublattice. *Int. J. Mod. Phys. B* 27, 1330002 (2013).
107. U. Daniel, M. Marinela, B. Radu, B. Raul, V. Nicolae, and C. Monica, Effect of the Mg substitution on the structural, optical, and electrical properties of $CuCrO_2$ for applications to *p*-type dye-sentsitized solar cells. NANOCON Brno, Czech Republic, EU, (2014) p. 390–394.
108. P. Lunca Popa, J. Crêpellière, R. Leturcq, and D. Lenoble, Electrical and optical properties of Cu-Cr-O thin films fabricated by chemical vapour deposition. *Thin Solid Films* 612, 194–201 (2016).

109. W. Ketir, S. Saadi, and M. Trari, Physical and photoelectrochemical characterization of $CuCrO_2$ single crystal. *J. Solid State Electrochem.* 16, 213–218 (2012).
110. M. Trari, J. Töpfer, P. Dordor, J.C. Grenier, M. Pouchard, and J.P. Doumerc, *J. Solid State Chem.* 178, 2751 (2005).
111. S. Mahapatra and S.A. Shivashankar, Low-pressure metal–organic chemical vapor deposition of transparent and *p*-type conducting $CuCrO_2$ thin films with high conductivity. *Chem. Vapor. Depos.* 9, 238 (2003).
112. S.N. Mott, *Conduction in Non-crystalline Materials* (Oxford: Clarendon Press, 1993), p.17ff.